JGR Planets

RESEARCH ARTICLE
10.1029/2022JE007450

Special Section:
The Mars Perseverance Rover Jezero Crater Floor Campaign

This article is a companion to Royer et al. (2022), https://doi.org/10.1029/2022JE007481.

Key Points:

- Mineralogy of rocks, regolith, and dust of the crater floor of Jezero, Mars was inferred from SuperCam reflectance data
- Assemblages suggest limited aqueous alteration of igneous rocks, followed by evaporation-induced deposition of sulfates
- Samples collected on the crater floor for return to Earth are representative of the geological diversity and witness past-aqueous processes

Supporting Information:

Supporting Information may be found in the online version of this article.

Correspondence to:

L. Mandon,
lucia.mandon@obspm.fr

Citation:

Mandon, L., Quantin-Nataf, C., Royer, C., Beck, P., Fouchet, T., Johnson, J. R., et al. (2023). Reflectance of Jezero crater floor: 2. Mineralogical interpretation. *Journal of Geophysical Research: Planets*, *128*, e2022JE007450. https://doi.org/10.1029/2022JE007450

Received 30 JUN 2022
Accepted 3 NOV 2022

Reflectance of Jezero Crater Floor: 2. Mineralogical Interpretation

L. Mandon[1], C. Quantin-Nataf[2], C. Royer[1], P. Beck[3], T. Fouchet[1], J. R. Johnson[4], E. Dehouck[2], S. Le Mouélic[5], F. Poulet[6], F. Montmessin[7], C. Pilorget[6], O. Gasnault[8], O. Forni[8], L. E. Mayhew[9], O. Beyssac[10], T. Bertrand[1], E. Clavé[11], P. Pinet[8], A. J. Brown[12], C. Legett[13], J. Tarnas[14], E. A. Cloutis[15], G. Poggiali[1,16], T. Fornaro[16], S. Maurice[8], R. C. Wiens[13,17], and The SuperCam Team[18]

[1]LESIA, Observatoire de Paris, Université PSL, CNRS, Sorbonne Université, Université de Paris, Meudon, France, [2]Université de Lyon, UCBL, ENSL, CNRS, LGL-TPE, Lyon, France, [3]Université Grenoble-Alpes, CNRS, IPAG, UMR 5274, Grenoble, France, [4]Johns Hopkins University Applied Physics Laboratory, Laurel, MD, USA, [5]Laboratoire Planétologie et Géosciences, CNRS UMR 6112, Nantes Université, Université Angers, Nantes, France, [6]Institut d'Astrophysique Spatiale, CNRS/Paris-Saclay University, Paris, France, [7]LATMOS, CNRS, Univ. Saint-Quentin-en-Yvelines, Sorbonne University, Guyancourt, France, [8]IRAP, CNRS, Université de Toulouse, UPS-OMP, Toulouse, France, [9]Department of Geological Sciences, UCB 399, University of Colorado Boulder, Boulder, CO, USA, [10]Institut de Minéralogie, de Physique des Matériaux et de Cosmochimie (IMPMC), Université Pierre-et-Marie-Curie (UPMC), Paris, France, [11]Centre Lasers Intenses et Applications, CNRS, CEA, Université de Bordeaux, Bordeaux, France, [12]Plancius Research, Severna Park, MD, USA, [13]Los Alamos National Laboratory, Los Alamos, NM, USA, [14]NASA, JPL, Caltech, Pasadena, CA, USA, [15]University of Winnipeg, Winnipeg, MB, Canada, [16]INAF-Astrophysical Observatory of Arcetri, Firenze, Italy, [17]Earth, Atmospheric, and Planetary Sciences, Purdue University, West Lafayette, IN, USA, [18]See Appendix A

Abstract The Perseverance rover landed in the ancient lakebed of Jezero crater, Mars on February 2021. Here, we assess the mineralogy of the rocks, regolith, and dust measured during the first year of the mission on the crater floor, using the visible and near-infrared spectrometer of SuperCam onboard the Perseverance rover. Most of the minerals detected from orbit are present in the bedrock, with olivine-bearing rocks at the bottom of the stratigraphy and high-Ca pyroxene-bearing rocks at the top. This is distinct from the overall low-Ca pyroxene-bearing composition of the watershed of Jezero and points toward an igneous origin. Alteration mineral phases were detected in most of the rocks analyzed in low proportions, suggesting that aqueous alteration of the crater floor has been spatially widespread, but limited in intensity and/or time. The diverse aqueous mineralogy suggests that the aqueous alteration history of the crater floor consists of at least two stages, to form phyllosilicates and oxyhydroxides, and later sulfates. We interpret their formation in a lake or under deeper serpentinization conditions and in an evaporative environment, respectively. Spectral similarities of dust with some rock coatings suggest widespread past processes of dust induration under liquid water activity late in the history of Jezero. Analysis of the regolith revealed some local inputs from the surrounding rocks. Relevant to the Mars Sample Return mission, the spectral features exhibited by the rocks sampled on the crater floor are representative of the diversity of spectra measured on the geological units investigated by the rover.

Plain Language Summary We present the results of the analysis of rocks and regolith measured during the first year after landing of the Perseverance rover on Mars. The analytical technique used is reflectance spectroscopy (the measurement of the light reflected by surfaces), which primarily provides information on mineralogy. The mineralogical composition of the magmatic rocks located near the landing site indicates that they have experienced several distinct episodes of interaction with water in the past, of relatively low intensity. Soil analysis reveals a composition similar to what has been observed at other sites on Mars, with a contribution from the disintegration of local rocks. The samples that are collected by Perseverance at the crater floor and brought back to Earth are representative of the diversity of the different geological units explored by the rover.

1. Introduction

The Noachian (>3.7 Ga in the Hartmann and Neukum (2001) chronology) and early Hesperian (3–3.7 Ga) terrains of Mars are marked by the activity of water, as evidenced by the presence of deltaic deposits, valley networks, and hydrated minerals (Carter et al., 2013; Fassett & Head, 2005; Mangold et al., 2021; Masursky, 1973; Poulet

et al., 2005). However, little is known about the duration and spatial extent of the liquid water activity on Mars. The science goals of the Mars 2020 mission (NASA) include characterizing past environments on Mars capable of supporting microbial life, searching for biosignatures, and collecting core rock and soil samples for return to Earth by the forthcoming Mars Sample Return (MSR, NASA/ESA) mission (Farley et al., 2020; Muirhead et al., 2020).

On 18 February 2021, the Mars 2020 rover Perseverance landed at the "Octavia E. Butler" site, on the floor of the 45-km diameter Jezero crater, which hosted a lake during Hesperian and/or Noachian eras (Fassett & Head, 2005; Mangold et al., 2021). During the first year of the mission, Perseverance investigated rocks and regolith of the crater floor with the aim of understanding the origin and history of its geological units. Before landing, it was uncertain whether the units of the crater floor were emplaced through magmatic/volcanic processes (such as lava flows or pyroclastic deposits) or as sediments related to the lake activity, and how they compared with the terrains of similar inferred mineralogy outside of Jezero.

The payload of Perseverance includes the SuperCam instrument, which combines several remote-sensing techniques to investigate the elemental and mineralogical composition of rocks and soils: high-resolution color imaging (Remote Micro-Imaging, RMI), laser-induced breakdown spectroscopy (LIBS), Raman spectroscopy, visible and near-infrared (VISIR) reflectance spectroscopy, and acoustic sensing (Maurice et al., 2021; Wiens et al., 2021). In particular, while near-infrared spectroscopy has been widely used to detect and map minerals from orbit (e.g., Carter et al., 2013; Ehlmann et al., 2009), its application as an in situ technique is a novelty. SuperCam passive reflectance spectra cover the 0.39–0.85 μm (VIS) and 1.3–2.6 μm (near-infrared or NIR) ranges, which allow the identification of a wide variety of minerals, especially hydrated ones, and hence can help to constrain past environmental conditions at Jezero crater (Fouchet et al., 2022).

In this contribution, we assess the mineralogy of the crater floor of Jezero using in situ SuperCam VISIR spectra acquired during the Crater Floor Campaign (until sol 379). Our analysis includes data collected on rocks (including cached samples) and soils at Jezero, and spanning a ∼1 km region around the landing site. We present observations of the Martian dust as well, measured for the first time in the near-infrared in situ. Our results have implications for the origin and alteration history of the rocks of the crater floor and open new possibilities for contextualizing orbital studies.

A companion paper describes the state of the calibration of the NIR data, as well as its impact on the detection of the minerals presented in this study (Royer et al., 2022).

2. Jezero Crater: Geologic Background

2.1. The Crater Floor and Its Watershed as Seen From Orbit

While several terrains explored by previous rover missions are of Hesperian age (e.g., Irwin et al., 2005), the particularity of Jezero crater is its Noachian age (Mandon et al., 2020) and hence the possibility to expose in-place Noachian rocks, providing insights into the earliest Martian environments. Its fluvial activity (continuous or intermittent) is likely to have started during the Noachian and persisted at least until the Early Hesperian (Mangold et al., 2020). The crater is connected to a large valley network, whose 15,000–30,000 km^2 catchment drained the Nili Fossae region, on the margin of the Isidis impact basin (Fassett & Head, 2005; Goudge et al., 2015). The main valley connected to Jezero crater, Neretva Vallis, dissects the Western rim and is associated with preserved deltaic deposits (Fassett & Head, 2005; Figure 1), which are likely to expose blocks of the Noachian crust for future exploration and sampling by the Perseverance rover (Mangold et al., 2021).

As seen from orbit, the area drained by this valley network shows abundant morphological and mineralogical diversity, and all of the various lithologies present in this region could have potentially been transported and deposited into Jezero in the delta region or as finer distal sediments in the lake. The most ancient rocks of the region, pre-Isidis impact (3.96 ± 0.1 Ga; Werner, 2008), can be observed as large massive or stratified basement outcrops or megabreccia blocks, with a spectral signature of low-Ca pyroxene or Fe/Mg-rich clays (Mustard et al., 2009; Scheller & Ehlmann, 2020). These lithologies are embedded in a low-albedo, smooth, and ridged phyllosilicate-bearing basement that is regionally capped by a ∼10 m thick Noachian-age unit found with olivine, carbonate and phyllosilicate mineral detections from orbit, hereafter referred to as the regional

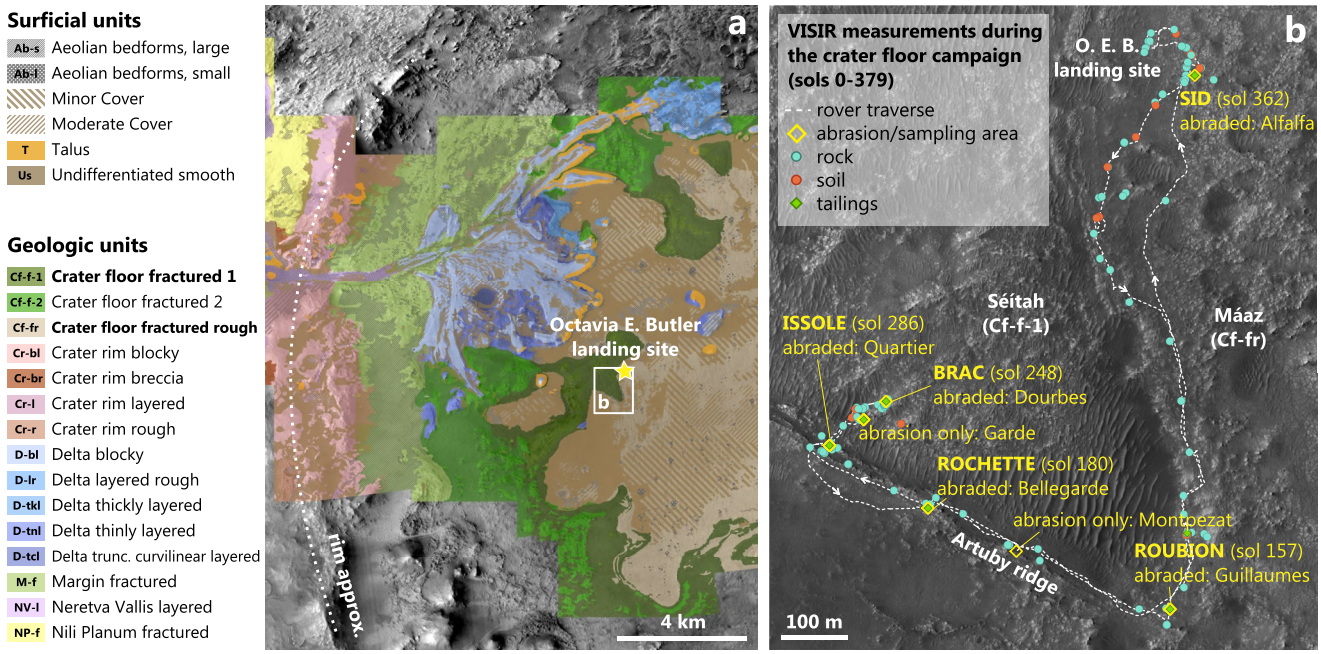

Figure 1. (a) Photogeological map of Western Jezero (modified from Stack et al. (2020)). (b) Rover traverse and reflectance measurement locations overlain on a High Resolution Imaging Science Experiment mosaic (Fergason et al., 2020; McEwen et al., 2007), SuperCam long-distance (>~60 m) observations excluded. Each color dot corresponds to a visible and near-infrared (VISIR) raster acquisition (usually consisting of one to 10 individual spectra spaced on a target), while diamonds correspond to VISIR raster on abrasion or sampling targets. Sol annotations next to an abrasion/sampling site refer to sol number arrival of the rover at the corresponding workspace.

olivine-bearing unit (Brown et al., 2010, 2020; Hoefen et al., 2003; Kremer et al., 2019; Mandon et al., 2020; Mangold et al., 2007; Mustard et al., 2007).

The interior of Jezero also shows morphological and mineralogical diversity, with spectral signatures similar to regional observations outside the crater (Goudge et al., 2015). In particular, the unit mapped by Stack et al. (2020) as the Crater floor fractured unit (Cf-f) and the Marginal fractured unit (Horgan et al., 2020) are fractured, light-toned, and have strong signatures of olivine and carbonate, respectively, all of these features being commonly observed in the regional olivine-bearing unit (Ehlmann et al., 2008; Goudge et al., 2015; Hoefen et al., 2003; Mustard et al., 2009; Ody et al., 2013; Figure 1). Stack et al. (2020) mapped the Cf-f unit as two distinct bedrock units: the Cf-f-2 occurs at higher elevation than the adjacent Cf-f-1 unit and exhibits a rougher texture with meter-scale bumps and ridges.

The Cf-f occupies the lowest position in the stratigraphy exposed at the crater floor. Kremer et al. (2019) and Mandon et al. (2020) showed that the regional olivine-bearing unit overlies the rim of Jezero crater, hence positioning both the regional olivine-bearing unit and the olivine-bearing Cf-f on the same stratigraphic level. However, from orbital studies, the relationship between the regional and Cf-f olivine-bearing units is ambiguous, and it is unclear if the olivine deposits inside and outside the crater share a common origin. From orbital studies, the following scenarios have been proposed to explain the nature of the regional olivine-bearing unit: lava flows (Tornabene et al., 2008), impact product of Isidis (Mustard et al., 2007; Palumbo & Head, 2018), pyroclastic deposits (Bramble et al., 2017; Kremer et al., 2019; Mandon et al., 2020; Rogers et al., 2018), and sedimentary deposits (Rogers et al., 2018). As noted by Stack et al. (2020), a volcanic, aeolian, or fluvio-lacustrine sediment origin appears plausible for the Cf-f unit, based on orbital data.

The Marginal fractured unit that outcrops on the Western part of the crater also shares morphological and spectral similarities with the regional olivine and carbonate-bearing unit. Horgan et al. (2020) proposed a distinct authigenic and lacustrine precipitation origin based on the strong carbonate signature and elevation distribution of the unit along the crater margin. The Perseverance rover has not yet investigated these exposures.

Stratigraphically above the Cf-f lies a unit referred to as the Crater floor fractured rough (Cf-fr) unit by Stack et al. (2020; Figure 1). This unit has a lower albedo than the Cf-f rocks, a rougher, boulder-producing, crater-retaining morphology and is associated with a spectral signature of pyroxene and olivine, which led Schon et al. (2012) and Goudge et al. (2015) to propose a lava flow origin for this unit. Because rocks with a similar morphology were observed from orbit and then interpreted as sediments with data from the Mars Science Laboratory (MSL) mission (Edgett, 2018), Stack et al. (2020) noted that a fluvio-lacustrine origin is also conceivable for the Cf-fr unit. The Cf-fr has been dated at 2.6 ± 0.6 Ga (Shahrzad et al., 2019), hence late in the crater history and after delta deposition. However, Quantin-Nataf et al. (2021) suggested that burying and resurfacing processes are responsible for this apparent young age. In their scenario, the Cf-fr would have been emplaced earlier (>3 Ga), before the deltaic exposures observed in the Western part of the crater. This hypothesis, also supported by Holm-Alwmark et al. (2021), has significant implications for sample return and calibration of the Martian chronology.

Overall, both the Cf-fr and the Cf-f-1 (explored by Perseverance during the first year of the mission) exhibit orbital spectral signatures of igneous minerals, with limited hydration, as opposed to the delta and the marginal fractured unit, or the geological units outside of Jezero crater, which exhibit stronger hydration features (Goudge et al., 2015).

2.2. Perseverance's Activities in the Crater Floor

The Perseverance rover landed at the Octavia E. Butler site, on top of the Cf-fr and close to the Cf-fr/Cf-f contact (Figure 1). During the first sols of the mission, the rover investigated rocks and soils of the Cf-fr that was informally renamed the Máaz formation ("Mars" in the Navajo language, in keeping with the naming scheme for the *Canyon de Chelly* quadrangle in which the rover landed). On sol 170, the rover reached an area with layered rocks named the Artuby ridge, and corresponding to the transition from the Cf-fr to the olivine-bearing Cf-f-1. On sol 202, the rover made its first entry into the Cf-f-1, in a highly dune-covered area called Séítah ("amidst the sands" in Navajo, Figure 1), and made its way back to the Octavia E. Butler area on sol 360 with the intent on driving to the delta front. Along the traverse, eight samples were successfully acquired, two pairs in the Máaz formation and two pairs in the Séítah formation (Simon et al., 2022).

The first ∼300 sols of investigation showed that the crater floor consists of igneous terrains and not lake sediments (Farley et al., 2022; Liu, Tice, et al., 2022; Wiens et al., 2022). They exhibit a density stratification, with decrease of the SiO_2 content and increase of FeO and MgO from the Máaz to the Séítah rocks (Wiens et al., 2022). In particular, mm-sized olivine crystals out of equilibrium with the melt composition and showing a poikilitic texture in Séítah suggest a cumulate origin (Beyssac et al., 2021; Liu, Tice, et al., 2022; Wiens et al., 2022).

2.2.1. The Máaz Formation (Cf-fr)

The Máaz formation is composed of dark-toned and massive rocks showing layering and internal stratification on its stratigraphically lowest portions (Horgan et al., 2023) and scarce vesicular texture, as well as flat, low-standing, and highly dust-covered rocks referred to as "pavers" (Figure 2a). These two types of rocks appear to be a different morphological expression of the same lithology, with the dark-toned rocks being likely more resistant to erosion than the pavers, as they share overall similar bulk-rock compositions (Udry et al., 2022; Wiens et al., 2022). Abraded rocks of the Máaz formation exhibits a texture showing angular coarse grains (>300 μm; Wiens et al., 2022) with no apparent matrix, and of variable tint (Figure 2b).

Elemental compositions point toward a basaltic composition for the Máaz formation, with dominant pyroxene, feldspar, and minor Fe-oxides and apatites (Razzell Hollis et al., 2022; Udry et al., 2022; Wiens et al., 2022). Secondary products were observed as bright salt deposits in the interstices of the Máaz formation rocks abraded patches *Guillaumes* and *Bellegarde*, likely consisting of Ca and Mg-sulfates, as well as anhydrous Na-perchlorates (Meslin et al., 2022; Razzell Hollis et al., 2022; Wiens et al., 2022). Rare occurrences of Fe/Mg-carbonates have also been found in these rocks (Clavé et al., 2022). An increase of the normative pyroxene proportion was observed at the lowest parts of the stratigraphy, in the Artuby ridge (Wiens et al., 2022).

2.2.2. The Séítah Formation (Cf-f-1)

As Perseverance drove along the Artuby ridge and the expected Máaz/Séítah contact, many layered rocks were observed, whereas they were rare within the Máaz formation itself. Séítah's outcrops exhibit thin (up to

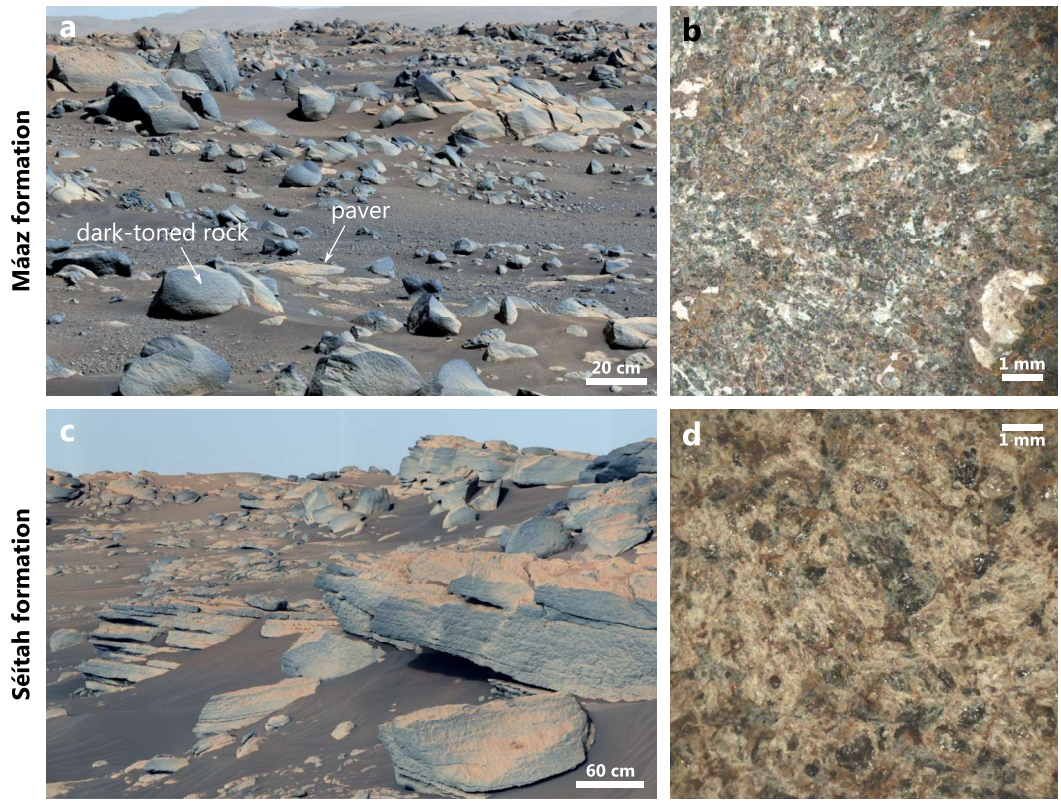

Figure 2. (a) Mastcam-Z mosaic panorama with the maximum zoom at 110 mm focal length taken on sol 78 in the Máaz formation. (b) Autofocus Context Imager (ACI) and Wide Angle Topographic Sensor for Operations and eNgineering (WATSON) merged images of the *Bellegarde* abraded patch (Máaz formation) taken on sol 186. (c) Mastcam-Z mosaic panorama with the maximum zoom at 110 mm focal length taken on sol 211 in the Séítah formation. (d) ACI and WATSON merged images of the *Garde* abraded patch (Séítah formation) taken on sol 207. See Supporting Information S1 for image IDs.

cm-scaled) nonplanar beds with a nodular appearance, usually capped by more massive beds of variable thickness (Figure 2c). A change of composition was recorded through the Máaz/Séítah contact, with increased Mg content (up to ~30% in Séítah; Wiens et al., 2022), detection of olivine in the lowest stratigraphic parts of Artuby and Séítah's rocks, and detection of carbonates (Beyssac et al., 2021; Clavé et al., 2022; Wiens et al., 2022). Abraded rocks in Séítah are coarse grained, and their texture and mineralogy are consistent with olivine-rich cumulates (Beyssac et al., 2021; Liu, Tice, et al., 2022; Figure 2d). Overall, Séítah's mineralogy is dominated by olivine and pyroxene, with scarce plagioclase, Fe-Ti oxides, Cr-rich Fe-Ti ulvospinel and some secondary alteration mineral phases like carbonates (Clavé et al., 2022; Liu, Tice, et al., 2022).

A few in-place outcrops near the top of the stratigraphy of Séítah differ in texture and composition from the surrounding layered, olivine-bearing rocks found in continuity. These outcrops consist of rocks of granular "pitted" texture, and lack olivine, with elemental compositions similar to the Máaz formation rocks (Udry et al., 2022; Wiens et al., 2022). They correspond to the rocks of the *Content* member described in Farley et al. (2022) and Wiens et al. (2022). Albeit these rocks being classified as part of the Séítah stratigraphy in these previous studies, here, we separate these pitted rocks from the nonpitted rocks of the Séítah formation due to their contrasting composition.

Both in the Máaz and Séítah formations, coatings were commonly observed on the surface of rocks. These coatings usually have a smooth texture and occur as discontinuous patches of variable thickness, with a purple tint on most enhanced color images (Garczynski et al., 2022). They show enrichment in Mg, S, and H compared to the rocks underneath (Wiens et al., 2022).

The techniques of LIBS (SuperCam instrument) and X-ray fluorescence (the Planetary Instrument for X-ray Lithochemistry, or PIXL instrument) allowed the quantification of rock chemistry based on major elements and the

detection of compositions compatible with the stoichiometry of minerals listed above. The use of VISIR spectroscopy complements these approaches by being particularly sensitive to the presence of hydrated and hydroxylated mineral phases, carbonates, sulfates, and iron-bearing phases ranging from iron oxides to olivines and pyroxenes (e.g., Bishop, 2020). It can assist in resolving some of the ambiguities of mineralogy that can arise when only the major elements are used and also detect minerals with low-Z elements (i.e., H and C) that can be challenging to identify with X-ray fluorescence or LIBS. Additionally, PIXL analyses are performed via contact with the targets, which limits the number of scans (mostly performed on abraded patches during the first campaign; Razzell Hollis et al., 2022). While the LIBS operates remotely, its capabilities are limited above ∼6.5 m distance from a target, where derived compositions are less reliable (Maurice et al., 2021; Wiens et al., 2021). The VISIR technique on the contrary is not limited by the distance and can measure spectra at long distances (theoretically, at infinity, as long as the atmospheric opacity can be adequately compensated), with a wider analysis spot than those of the LIBS. Indeed, the field of view of the VISIR spectrometer is on the order of 1.4–2.3 mm for a mast-to-target distance of 2 m, while the surface ablated by the LIBS is on the order of <0.5 mm. As the technique does not use a laser like the LIBS or Raman techniques, it can be operated regularly with relative limited power, as long as the target is sunlit. The main minerals detected during the first year of the mission with the VISIR technique have been reviewed in Wiens et al. (2022); the goal of our study is to present them extensively as well as their significance for our understanding of the formation and evolution of rocks at Jezero crater.

3. Data Set and Processing

3.1. VISIR Reflectance Spectroscopy

Reflectance spectroscopy, that is, the measurement of the VISIR light (∼0.4–4 μm) reflected and scattered by the first microns of a surface, is a nondestructive technique that has been widely used in planetary science. In particular, investigation of the reflectance in the 1–2.6 μm range has allowed the detection and mapping of a breadth of minerals on the surface of Mars, including mafic minerals (olivine and pyroxene), iron oxides, feldspar (detectable in NIR if Fe-bearing), a variety of hydrous minerals (including phyllosilicates, sulfates, hydrated silica, zeolites, epidote, and prehnite), and carbonates (e.g., Brown et al., 2010; Carter & Poulet, 2013; Carter et al., 2013; Ehlmann et al., 2008, 2009; Gendrin et al., 2005; Hoefen et al., 2003; Mustard et al., 2005; Poulet et al., 2005; Roach et al., 2010).

The combined techniques of VISIR provide high sensitivity to the presence of Fe-bearing minerals, due to electronic transitions absorption bands related to transition elements. In the visible wavelengths, crystalline ferric oxides exhibit absorptions near 0.53–0.54 μm and a ferric oxide absorption edge near 0.60 μm that is particularly evident on Mars owing to the ubiquitous presence of oxidized dust. This results in reddened spectra in the visible range, with reflectance maxima typically near 0.75 μm, sometimes followed by downturns toward the near-infrared. Some ferric oxide minerals and hydrated iron-bearing sulfates have prominent absorptions in this 0.80−0.86 μm region. Reflectance downturns toward the near-infrared are also attributable to ferrous iron absorption bands in olivine and pyroxene, which are often also associated with shorter-wavelength peak reflectance maxima (<0.7 μm) (e.g., Bell et al., 2008; Johnson et al., 2015). In the near-infrared, electronic absorptions centered around 1 μm occur for most Fe-rich minerals and around 1 and 2 μm in the specific case of pyroxene (Burns, 1993; Clénet et al., 2011; Cloutis & Gaffey, 1991; Klima et al., 2007). Though the 1 μm band center is outside of SuperCam' spectral ranges, these bands are large enough that the high-wavelength wing produces a strong red slope at the shortest NIR wavelengths probed by SuperCam, and the low-wavelength wing can be observed partially by the longest SuperCam VIS wavelengths. Mastcam-Z multispectral observations (0.44–1.02 μm) provide additional information in this region (e.g., Johnson et al., 2022; Horgan et al., 2023; Rice et al., 2023).

The near-infrared is highly sensitive to the presence of alteration minerals, as the combinations and overtones of bending and stretching of groups such as H_2O, metal-OH, CO_3^{2-}, and SO_4^{2-} in minerals cause various narrow absorptions in the near-infrared. In particular, H_2O-bearing minerals spectra exhibit absorption bands centered around ∼1.4 and ∼1.9 μm. The 1.4 μm region can also exhibit an absorption feature due to OH. Shallow absorptions centered in the 2.1–2.5 μm range allow the discrimination of additional molecular bonds: around 2.2 μm with the presence of Al–OH, Si–OH, and Si–O–Si, 2.28 μm for Fe^{3+}–OH, 2.35 μm for Fe^{2+}–OH, and 2.1 and 2.32 μm for Mg–OH. The CO_3^{2-} group is identified with the codetection of absorptions centered at ∼2.3 and 2.5 μm, while SO_4^{2-} usually induces absorptions around ∼1.7 and 2.4 μm. Variability in band position can be observed

with compositional change (and to a lesser extent, grain size variation), and mineralogical identification is usually performed by comparing the number and position of absorptions of a measured spectrum to those of reference spectra obtained in laboratories.

3.2. The VISIR Spectrometer of SuperCam

SuperCam is divided into two main units: a body unit (BU), which includes three spectrometers used to measure the UV and visible light and that are primarily used by the LIBS technique, and a mast unit (MU), which hosts the infrared spectrometer (IRS). One of the three BU spectrometers is used to produce the VIS spectra shown here: the transmission spectrometer, which covers the visible 0.535–0.855 μm range in 6,000 channels and with a varying FWHM spectral resolution of 0.3–0.4 nm (Wiens et al., 2021). This spectrometer uses three regions: Green (0.535–0.620 μm), Orange (0.620–0.712 μm), and Red (0.712–0.853 μm). Data provided by the blue-violet (VIO) spectrometer provide information for the short wavelength (0.379–0.464 μm) region but corresponding reflectance spectra have a relatively low signal-to-noise ratio. The near-infrared range is covered by the IRS, an acousto-optic tunable filter (AOTF) spectrometer located in the MU and which operates by scanning the light between 1.3 and 2.6 μm, along 256 channels (spectels) and with a spectral resolution of 32 cm^{-1} (around 5 nm at 1.3 μm, 11 nm at 1.95 μm, and 20 nm at 2.6 μm; Fouchet et al., 2022). Every SuperCam activity on a target consists of a "raster," that is, a set of "points" (usually from one to 10), each being associated with a LIBS, Raman, VISIR spectrum, and/or RMI image. Whenever a LIBS activity was performed along with reflectance spectroscopy for a rock target, the VISIR spectra are acquired after the LIBS bursts, in order to take advantage of partial dust removal performed by the LIBS plasma (Maurice et al., 2016). For soils, the VISIR data are acquired prior to the LIBS to avoid effects of shadowing in the resulting LIBS pits. The analytical footprint of VISIR is much larger than the LIBS ablation spot on the target surface. Therefore, any structural damage due to the prior LIBS analyses on the sample is considered negligible in the VISIR data. This was demonstrated by Fau et al. (2019) for the SuperCam Raman data that have a similar analytical footprint to VIS spectroscopy and slightly smaller than for the NIR spectroscopy (Maurice et al., 2021).

The light that enters the spectrometers is collected by a Cassegrain telescope in the MU, with a field of view of 0.7 mrad for the visible spectrometer and 1.15 mrad for the IRS (Maurice et al., 2021). This corresponds to a ∼1.4 and ∼2.3 mm footprint, respectively, for a mast-to-target distance of 2 m. At this scale, several individual mineral phases can be present in the field of view of the instruments, and the measured VISIR spectra are often combinations of different spectral components. The footprint center of the IRS is offset by 0.3 mrad with regard to the other spectroscopy techniques of SuperCam that operate using the optical fiber that collects light to the BU (VIS reflectance, LIBS, and Raman; Maurice et al., 2021).

3.3. Calibration Overview

3.3.1. Calibration of the Visible Spectrometer

For VIS data used here, 50 spectra were averaged for each point. Raw VIS data were converted to radiance via an instrument transfer function derived from lab measurements with an integrating sphere (Maurice et al., 2021; Wiens et al., 2021). Relative reflectance spectra were generated by dividing the calibrated target radiance spectrum by a radiance spectrum of the onboard AluWhite SuperCam Calibration Target (SCCT), whose reflectance properties are well known (Cousin, Sautter, et al., 2022). An AluWhite spectrum taken on sol 20 was used as this reference up to sol 129, when the number of rows summed for the Red portion of the transmission spectrometer was updated for all subsequent spectra. Afterward, only the first spectrum from the sol 184 set was used for calibration of postsol 129 data, resulting in improved spectra (Legett et al., 2022). Residual issues in the VIS spectra include the narrow Cr^{3+} AluWhite emission feature at ∼0.694 μm (removed by interpolating the plotted spectra in this contribution) and decreased sensitivity near detector boundaries for Green/Orange (∼0.62 μm) and Orange/Red (∼0.712 μm), which can cause offsets and artifacts. Finally, relative reflectance spectra were geometrically scaled to the relevant illumination conditions by multiplying by the Mars-to-Sun distance and Solar incidence cosine ratios.

3.3.2. Calibration of the IRS

The calibration of the IRS is detailed in a companion paper (Royer et al., 2022) and includes dark smoothing and subtraction, reflectance conversion (also accounting for the radiometric and geometric correction), atmospheric

correction, and optical throughput as a function of temperature. The processing also includes removal of "glitches" (anomalously low values induced by drops of the radio frequency signal supplying the transducer of the instrument) and "spikes" (anomalous values generated by the readout electronics) of the radiance data. The atmospheric correction is performed by dividing the reflectance data by $t_{CO_2}^k$, where t_{CO_2} is an atmospheric transmission model and k is a constant adjusted to minimize the CO_2 main absorption feature around 2 μm. The spectral calibration was performed before the flight during the instrument production. The wavelength fluctuation varies as a function of the AOTF temperature but was estimated to be very minor (5–15 nm within a 50°C range).

The calibrated and corrected data are affected by residual instrumental effects mainly related to the temperature of the IRBoard (the electronic component driving the IRS and located in the electronic box of the MU) and the optical box (OBOX, where the IRS is located). Though largely corrected by using AluWhite spectra at different IRBoard temperatures (Royer et al., 2022), this dependency can still affect some spectra by inducing low-frequency reflectance variations near ∼1.7, ∼2.3, and >∼2.55 μm. However, these residuals have been estimated by Royer et al. (2022) to be minor and acceptable for mineralogical identification.

3.4. Data Analysis

A VISIR observation (referred to as a raster) usually consists of one to ten single-point spectra. As stated previously, the field of view of the spectrometer is a few mm-wide and as it is commonly the case in planetary spectroscopy and for other techniques as well, the measured spectra are the results of the complex mixture of the spectral signatures of each different mineral phases present in the field of view. Hence, the probability that a single type of mineral was observed in a single point is low, and the measured spectra are most likely to be combinations of different components. Additionally, the spectral predominance of some minerals can be an issue for identification. Indeed, spectral mixing of mineral signatures are nonlinear with proportion, and spectral measurements on laboratory mixtures have demonstrated that a few percent of particular mineral phases can in some cases have a strong impact on the spectral information in the near-infrared (e.g., Bishop et al., 2013; Mandon, 2020; Mandon et al., 2022).

We carried out a spectral analysis to (a) identify spectral endmembers that could be indicative of mineralogical endmembers and (b) estimate the distribution of the various identified minerals along the traverse and specific outcrops. Here, we present several data types. The majority of the spectra shown in this contribution are single-point or mean target spectra. These spectra are usually the result of the complex mixing of different mineral phases: in order to highlight the contribution of isolated minerals, we performed spectral ratios for specific observations and applied Independent Component Analysis (ICA) to some subsets of the data. These methods are described in the two following sections.

3.4.1. Spectral Ratios

The use of spectral ratios is commonly performed on orbital imaging spectrometers data to highlight the spectral signatures of particular minerals occurring as mixture in the pixels (e.g., Carter et al., 2015; Ehlmann et al., 2009; Horgan et al., 2020; Viviano-Beck et al., 2014). To this aim, a spectrum of a region of interest is divided by the spectrum of a nearby, spectrally neutral region (i.e., exhibiting no specific absorption bands). Another possibility for orbital data is the use of the detector column median spectrum as a denominator when there are column-dependent artifacts (e.g., Mandon, Parkes Bowen, et al., 2021), typically for instruments operating in pushbroom mode, such as the Compact Reconnaissance Imaging Spectrometer for Mars instrument (CRISM; Murchie et al., 2007). The ratioing method allows to highlight spectral features while minimizing the contribution of the atmosphere and aerosols (dust and clouds).

Normalization of SuperCam VISIR data was performed for a few observations (stated in the figures when applied) by ratioing the spectrum of a point by the median of the raster. The median is usually not spectrally neutral, but the normalization allows to highlight faint absorptions that are specific to mineral phases with varying proportions relative to others in the raster.

3.4.2. Independent Component Analysis

The second method is Independent Component Analysis (ICA). In this approach, a number of multivariate signals (a suite of measured IRS spectra) are separated into different sources, in order to try to isolate endmember mineral spectra. Here, the sources are nondependent and non-Gaussian, while the mixed signals are both. The ICA aims at identifying the least Gaussian and more independent components from the measured spectra; in other words, the spectral signals that describe best the variability observed in a set of reflectance spectra.

In this work, the Joint Approximate Diagonalization of Eigenmatrices (JADE; Cardoso & Souloumiac, 1993) ICA algorithm was implemented on several parts of the IRS spectral database of SuperCam, with a fixed number of components n. Indeed, an assumption was made on the number of independent components that contribute to the spectra. As ICA components are not reflectance spectra per se, some may be difficult to interpret. We found that for SuperCam IRS data, n equal to two or three provides the individual components that are the more easily interpretable in terms of the minerals present (i.e., with loadings that compare the best to spectra of natural samples measured in laboratories). A unique feature of the JADE algorithm is the use of kurtosis as a non-Gaussian criterion, which measures the dispersion of the probability weights relative to the center of distribution.

While ICA decomposition aims at providing physically/chemically significant components, some caveats are associated with this method. First, there is no determination of sign or amplitude of the sources. Additionally, the method is inadequate to identify individual Eigen spectra in homogenous targets (e.g., borehole tailings, whose spectra show less intraraster variability). The results are also model-dependent; nevertheless, the JADE algorithm results shown in this contribution were compared to the results obtained with the Fast-ICA algorithm (Hyvärinen & Oja, 2000), which returned similar individual components.

3.4.3. Absorption Bands Retrieval and Main Spectral Parameters

3.4.3.1. Determining Absorption Band Parameters

For all the point spectra, we measured the position of the absorption centers by performing the following steps, described in Mandon et al. (2021) with an example shown in Figure S1 in Supporting Information S1: first, the single-point spectra were lightly denoised using wavelet denoising (using a soft BayesShrink algorithm), then a spectral continuum was fitted using the upper part of a convex hull of the NIR-only spectrum. This step was repeated until all band shoulders were satisfactorily included in the continuum. Then, the continuum was divided from the data, allowing determination of the center and depth (one minus the minima of the continuum-removed spectrum) of the various absorption bands.

3.4.3.2. Other Spectral Parameters

To evaluate the broad spectral diversity of all observations, we measured the spectral slopes in the 1.3–1.8 and 2.1–2.5 μm ranges, with band centers at 1.3 and 2.1 μm and assuming a linear continuum shouldered at 1.8 or 2.5 μm (Table 1). Together, these parameters allow a first-order evaluation of the contribution of different mineral families. Here, olivine exhibits a strong and positive 1.3–1.8 μm slope with a 2.1–2.5 μm slope close to zero. As the band centers and shoulders of the ∼1 and ∼2 μm bands of pyroxene shift with Ca/Fe/Mg relative proportion in the crystals, the values of these parameters are expected to vary with both pyroxene abundance and composition. Low-Ca pyroxenes have a negative 1.3–1.8 μm slope and a positive 2.1–2.5 μm slope, while these slopes are both positive in the case of high-Ca pyroxenes. Hydrated minerals have a negative 2.1–2.5 μm slope owing to water-related absorption. Spectra of Fe-bearing minerals exhibit a positive 1.3–1.8 μm slope as well, though its intensity is weaker in the case of Fe^{3+} compared to Fe^{2+}, the latter inducing a stronger absorption near 1 μm. For non-Fe-bearing hydrated minerals, this slope is usually close to zero.

For the SuperCam VIS spectra, simple ratios and spectral slope parameters were used in the same manner as was done with MSL ChemCam passive spectra to distinguish different types of soil and rock materials (e.g., Johnson et al., 2015). For example, overall "redness" (0.67/0.44 μm ratio) or the magnitude of the near-infrared drop off (0.75–0.84 μm slope) helped resolve variations in ferric versus ferrous components. Comparisons of spectral slopes and ratios between 0.60 and 0.84 μm provided some sensitivity to dust coatings. Band depths at 0.545 μm provided a means to track the influence of crystalline ferric materials and were computed using shoulders at 0.60 and 0.43 μm (Clark & Roush, 1984). When calculating these spectral parameters, the average relative reflectance value for a given wavelength was computed using all channels within ±5 nm of that wavelength.

Table 1
List of the Main Spectral Parameters Used in This Study

Parameter	Value	Sensitivity	Appears in figure(s)
0.545 μm band depth[a]	$1 - R/R_c$ where R is the value of the reflectance spectrum at 0.545 μm and R_c the value at 0.545 μm of the continuum anchored at 0.43 and 0.60 μm	Crystalline ferric materials	Figure 5
0.67/0.44 μm ratio[a]	$R_{0.67\ \mu m}/R_{0.44\ \mu m}$	"Red" surfaces	Figure 5
0.75–0.84 μm slope[a]	Slope between 0.75 and 0.84 μm	Mafic minerals and other Fe-bearing mineral phases	Figure 5
0.60–0.84 μm slope[a]	Slope between 0.60 and 0.84 μm	Dusty surfaces	Figure 5
1.3–1.8 μm slope	$1 - R_{1.34\ \mu m}/R_{1.80\ \mu m}$	• Strongly positive for olivine, high-Ca pyroxene and other ferrous mineral phases, moderately positive for ferric minerals • Negative for low-Ca pyroxene	Figures 9 and 10
2.1–2.5 μm slope	$1 - R_{2.15\ \mu m}/R_{2.5\ \mu m}$	• Negative for water-bearing mineral phases • Positive for pyroxene	Figure 10
2.13 μm band depth	$1 - R/R_c$ where R is the value of the reflectance spectrum at 2.13 μm and R_c the value at 2.13 μm of the continuum anchored at 1.93 and 2.18 μm	Kieserite	Figure 7

Band identified in the CRS	Band position range	Sensitivity	Appears in figures
1.9 μm band	1.90–2.0 μm	H_2O, OH	Figures 7 and 9
2.28 μm band	2.26–2.295 μm	Fe^{3+}–OH	Figures 7 and 9
2.3 μm band	2.26–2.35 μm	Fe–OH, Mg–OH, carbonate	Figures 7 and 9

Note. The NIR parameters are computed on the denoised spectra (see Section 3.4.3). The last section of the table lists the spectral range considered to classify some of the absorptions identified once the continuum was removed from NIR data. CRS: continuum-removed spectrum, R_λ: reflectance at a given wavelength λ
[a]See Johnson et al. (2015).

3.5. Context Images

In this contribution, context and location of VISIR measurements are given from the various color imaging instruments of the rover: the SuperCam RMI (Gasnault et al., 2021; Wiens et al., 2021), the Mast Camera Zoom (Mastcam-Z; Bell et al., 2021), the Wide Angle Topographic Sensor for Operations and eNgineering (WATSON; Bhartia et al., 2021), and the Hazard Avoidance Cameras (Hazcams; Maki et al., 2020). The RMI produces Bayer-filter images in a 18.8 mrad footprint (less than 4 cm for a mast-to-target distance of 2 m), at a resolution of 10 μrad/pixel and with a narrow depth of field (Maurice et al., 2021; Wiens et al., 2021). The Mastcam-Z instrument is a set of two zoomable cameras (with a focal length ranging from 26 to 110 mm) that produce broadband Red/Green/Blue color stereo-images as well as multispectral reflectance spectra in the 0.4–1 μm range (Bell et al., 2021). WATSON is a camera built on the heritage of the MSL Mars Hand Lens Imager camera and mounted on the rover robotic arm, allowing proximity imaging of targets in the close environment of the rover (Bhartia et al., 2021). The associated images have a resolution ranging from ∼13 μm/pixel to infinity depending on standoff distance to the target. WATSON is coupled with the Autofocus Context Imager (ACI), which acquires ∼10 μm/pixel grayscale images. Finally, additional context was provided by the Hazcams color images at 0.46 mrad/pixel (Maki et al., 2020). In this contribution, RMI, WATSON, and ACI images are used to show target texture, while Mastcam-Z and Hazcams color images are shown for wider context (e.g., whole rock imaging).

The list of image IDs shown here is found in Text S1 in Supporting Information S1.

4. Results

As of sol 379, nearly 2000 interpretable VISIR spectra (i.e., without saturation or major shadowing in the field of view) were acquired on targets in the nearby rover environment, including ∼1,400 spectra on ∼150 unabraded rock targets, ∼300 spectra on ∼20 soil targets, ∼150 spectra on seven abraded patches of rocks, and ∼120 spectra

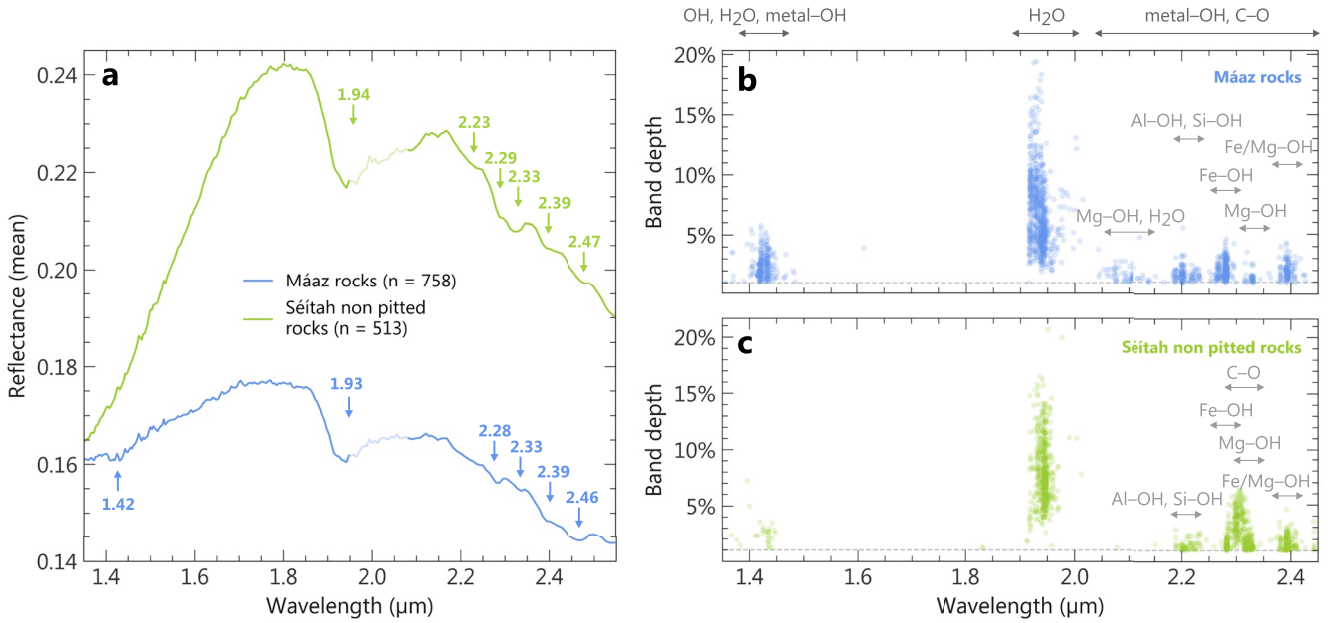

Figure 3. Near-infrared spectral signature of the rocks of the crater floor (until sol 379). (a) Mean spectra of rocks of the Máaz and Séítah formations. Parts of the spectra near 2 μm shown with lower opacity correspond to the main atmospheric CO_2 absorption domain, where correction residuals might affect the spectra. (b and c) Position and depth of the absorption bands extracted on the Máaz (b) and Séítah (c) rock spectra after continuum removal (with a threshold of 1% absorption, in agreement with a SNR of 100, met in the majority of the observations; Royer et al., 2022). The spectral ranges of absorptions of interest are indicated with light gray arrows. Because of the thermal sensitivity of the infrared spectrometer past ~2.5 μm, no band centered after 2.45 μm is shown as their position might be affected by this caveat. All the absorptions detected near 1.4 μm and in the 2.1–2.5 μm range are associated with an absorption near 1.9 μm.

on 13 tailings of coring or abrasion (Figure 1). The list of the VISIR observations used in this contribution along with the sol of execution of the activity can be found in Table S1.

Most of the spectra measured on rocks of the crater floor exhibit an absorption near 1.9 μm, indicating the presence of water (Figure 3). More precisely, 94% of individual spectra on rock targets of the crater floor show a >1% band depth absorption (relative to the continuum) near 1.9 μm, and the median 1.9 μm band depth is 7% (relative to the continuum). Additional shallower bands in the 2.1–2.4 μm range indicate the presence of secondary minerals (Figure 3). The Máaz and Séítah formation rocks exhibit distinct spectral signatures, indicative of different primary and secondary mineral assemblages, as detailed in the following sections. The summary of all the mineral phases identified based on VISIR spectroscopy is shown in Table 2.

4.1. Dust and Coatings

4.1.1. Dusty Rocks

The Martian dust is a ubiquitous cover of all surfaces and is known to affect the reflectance spectra measured on rocks—mostly by inducing a red spectral slope in the visible and flattening the spectra in the near-infrared (e.g., Le Mouélic et al., 2006). However, before SuperCam operations on Mars, no in situ measurement had been performed in the 1.3–2.6 μm near-infrared range. On sol 141, an experiment was conducted on the target *Salles* by acquiring VISIR spectra before and after LIBS measurements in order to assess the influence of the LIBS dust removal on the VISIR spectra. Subtle differences in the VISIR spectra were noted, including a blueing of the reflectance in the VIS range as dust is usually redder compared to rocks (see Figure S2 in Supporting Information S1), similar to the results obtained by MSL ChemCam instruments on dusty rock target but in that case limited to the visible range (Johnson et al., 2015). However, investigation of the RMI images shows that dust removal was minor on this target, limiting the possible interpretation.

We present in Figure 4a the VISIR single-point spectra of the dustiest surfaces measured during the crater floor campaign. One of the dustiest surfaces (based on RMI images) was observed on the *Naltsos* target, a paver with a strong 0.545 μm band depth related to crystalline and/or nanophase ferric oxides (Figure 4b). Figure 5d presents a

Table 2
Summary of the Minerals Non-Ambiguously Identified With the Visible and Near-Infrared Spectrometer of SuperCam on the Crater Floor of Jezero and Corresponding Spectral Features (Values Are Absorption Centers)

Máaz		Clinopyroxene[a,b]	~2.3 μm (broad and wide; ICA)
		Fe-oxyhydroxide(s) (e.g., ferrihydrite, akaganeite[c])	1.93–1.94 μm (wide), occasional 2.46 μm (point spectra and ICA)
		Fe^{3+}-phyllosilicate (nontronite or hisingerite likely)	1.42, 1.92, 2.28–2.29, and 2.39 μm (point spectra and ICA)
		Monohydrated Mg-sulfate	2.13 and 2.4 μm downturn (occasional; point spectra, ratios)
		Al or Si–OH-mineral (Al-phyllosilicate and/or hydrated silica)	2.20–2.22 μm (point spectra)
		Mg–OH mineral (smectite, serpentine, talc, and/or brucite) and/or carbonate—minor	2.32–2.33 μm (point spectra)
Séítah	Pitted	Fe-oxyhydroxide(s) (e.g., ferrihydrite)	1.93–1.94 μm (wide; point spectra)
		Fe^{3+}-phyllosilicate (nontronite or hisingerite)	1.42, 1.92, 2.28–2.29, and 2.39 μm (point spectra)
	Nonpitted	Olivine[a,b]	0.7–1.8 μm range (broad; point spectra and ICA)
		Clinopyroxene	~2.3 μm (broad and wide; ICA)
		Fe^{3+}-mineral (nontronite or hisingerite)[b]	2.28–2.29 μm (point spectra and ICA)
		Mg–OH mineral (Mg-smectite, serpentine, talc and/or brucite)[b]	2.32–2.33 μm (point spectra and ICA)
		Fe/Mg-carbonates[a,b]	2.53 μm (point spectra)
		Fe-oxyhydroxide(s) (e.g., ferrihydrite)	1.93–1.94 μm (wide; point spectra)
		Monohydrated Mg-sulfate	1.9–2.3 μm (ratios)
		Al or Si–OH-mineral (Al-phyllosilicate and/or hydrated silica)[b]	2.20–2.22 μm (point spectra)
Soils	Fine (μm-sized)	Pyroxene	~2 μm (broad and wide; point spectra and ICA)
		Olivine	0.7–1.8 μm range (broad; point spectra and ICA)
		Hydration	1.94 μm (point spectra and ICA)
	Coarse (μm–mm-sized)	Olivine	0.7–1.8 μm range (broad; point spectra and ICA)
		Fe^{3+}-mineral (nontronite or hisingerite likely)	2.28–2.29 μm (point spectra and ICA)
		Mg–OH mineral (Mg-smectite, serpentine, talc, and/or brucite)	2.32–2.33 μm (point spectra and ICA)
Dust		Fe-oxides	Strong 0.545 μm band depth and 0.60–0.84 μm slope (point spectra)
		Hydration	1.94 μm (point spectra)
Purple coatings		Fe-oxides	Strong 0.545 μm band depth and 0.60–0.84 μm slope (point spectra)
		Hydration	1.94 μm (point spectra)

Note. Other suspected minerals are discussed in the text. Items labeled with a number in the Máaz and Séítah sections indicate minerals that have been detected in the corresponding unit from orbital NIR spectroscopy.
[a]Goudge et al. (2015). [b]Horgan et al. (2020). [c]Carter et al. (2022).

comparison of 0.60–0.84 μm spectral slopes versus 0.60/0.84 μm ratio, which was shown by Johnson et al. (2015) to be a useful proxy for ferric dust coatings on spectrally neutral, low-albedo substrates. Here, *Naltsos* plots as one of the dustiest endmembers of the Máaz targets (compared to the least dusty targets such as *Manior*).

Based on visual investigation of color and texture of rocks in RMI images, 13 points with thick dust coating covering the whole SuperCam VISIR field of view were identified. The average spectrum from these observations is presented in Figure 4a. In the infrared, these dusty surfaces exhibit a relatively flat spectrum, with a faint absorption related to hydration at 1.93 μm (~3%–5% of absorption relative to the continuum) as well as a subtle downturn after ~2.3 μm, attributable to a number of poorly crystalline water-bearing mineral phases (Figure 4). While the 1.9 μm absorption might be caused by hydrated material of the rock underneath the dust cover, analysis of corresponding Mastcam-Z and RMI images shows optically thick coating of dust in most of the field of view,

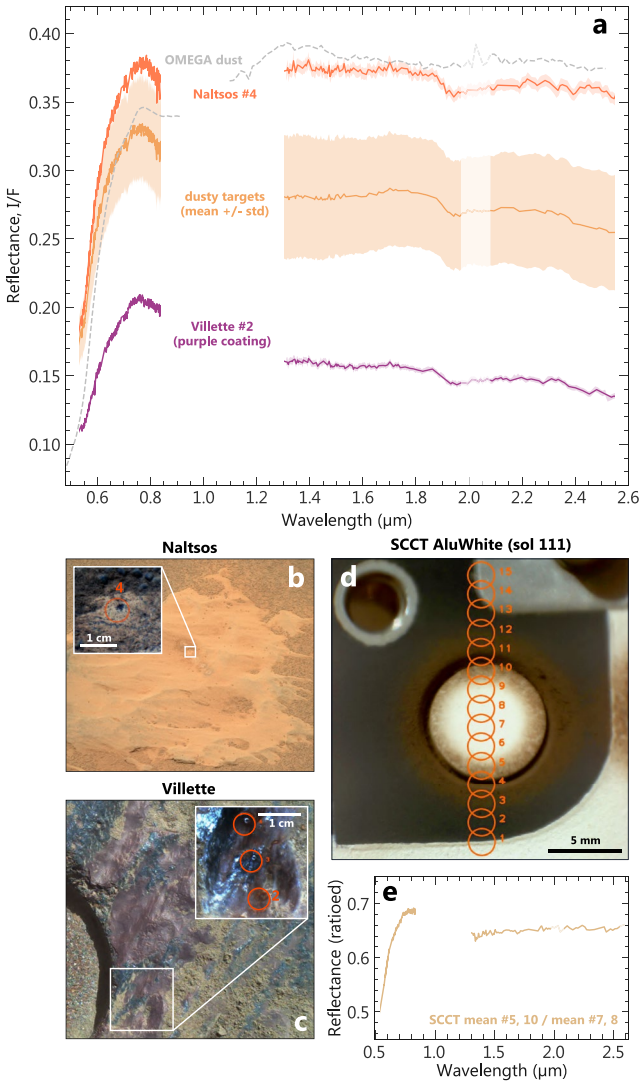

Figure 4. Visible and near-infrared signature of dust-covered targets and coatings. (a) Mean spectrum of 13 points where significant dust coatings have been observed based on Remote Micro-Imaging (RMI) images (list in Text S3 in Supporting Information S1), spectrum of location #4 on the highly dusty paver *Naltsos* with corresponding Mastcam-Z image and RMI close-up in panel (b), and spectrum measured on location #2 of the target *Villette* coated by purplish material, with corresponding Wide Angle Topographic Sensor for Operations and eNgineering (WATSON) image and RMI close-up in panel (c). For comparison, an Observatoire pour la Minéralogie, l'Eau, les Glaces et l'Activité orbital measurement of a dusty terrain north of Syrtis Major (Le Mouélic et al., 2006) is shown. (d) RMI image and infrared spectrometer (IRS) pointing of a vertical observation showing dust accumulation associated with magnetized region around the SuperCam Calibration Target (SCCT) AluWhite reflectance standard. Red circles indicate the location of the field of view of the IRS accounting for 68% of signal. (e) Ratioed spectrum of the SCCT edges covered in dust over the measurements centered in the middle of the SCCT shown in panel (d), highlighting the spectral signature of the magnetic dust deposited on the edges of the SCCT. Segments of the spectra shown with lower opacity line near 2 μm correspond to the main atmospheric CO_2 absorption domain, where residuals might affect the spectra. See Text S1 in Supporting Information S1 for image IDs.

likely to mask any spectral signature originating from the rock (Figure 4b). Additionally, nearly all SuperCam dusty targets (mainly pavers) exhibit a 1.9 μm region absorption band.

4.1.2. Recently Deposited Dust

After the rover's landing, airborne dust started to accumulate on the rover deck and on each SCCT, providing the opportunity to investigate the properties of the recently deposited dust. Several of the SuperCam reflectance calibration targets are enclosed in a magnetic ring, intended to deflect the magnetic fraction of airborne dust from the center to the edge of the SCCT (Manrique et al., 2020). On sols 72 and 111, two VISIR observations were performed on the AluWhite SCCT to check the horizontal and vertical alignment of the IRS, measuring both the center of the SCCT and its magnetic dust-covered edges (Figure 4). Similar to dust-coated rocks, the spectra of the AluWhite SCCT recently covered by the magnetic fraction of the airfall dust exhibit a strong red slope in the visible. However, unlike the typical dust-coated rocks or soils, the VIS spectra exhibit only a weak 0.545 μm band and a positive 0.75–0.84 μm spectral slope. Merusi (2022) provide additional multispectral observations of the magnetic dust using Mastcam-Z data (0.44–1.02 μm). In the IRS data, no clear absorption was observed in the near-infrared range (Figure 4e).

4.1.3. Coatings

The purple-tinted material found as coatings on the rocks of the crater floor has been investigated by SuperCam. Only one example is shown here, on the target *Villette*, but Garczynski et al. (2022) showed that the rock coatings of the crater floor share similar reflectance spectra in the VISIR. Interestingly, these purple-tinted coatings share similar features with the dust-covered surfaces. While they are darker than dusty rocks over the whole VISIR range, their spectra likewise show a red slope in the ~0.6–0.8 μm range, among the strongest 0.545 μm band depths, as well as relatively flat shapes in the NIR, along with faint 1.93 μm absorption and downturn longward of ~2.3 μm (Figures 4a and 4c). These spectral similarities suggest similar composition and a link between the modern Martian dust and the purple coating observed at Jezero crater, as discussed further in this contribution and by Garczynski et al. (2022). We note that these coatings are not present on all rock targets and cannot explain the pervasive presence of an H_2O band in VISIR data of rocks.

4.2. Rocks of the Máaz Formation

In the Máaz formation, the single-point spectra of the dark-toned rocks (i.e., the least-dusty rocks) most often exhibit a concave shape in the infrared range, with a pronounced 1.9 μm water absorption centered between ~1.92 and 1.95 μm. The strongest water bands were observed in point spectra of the *Bidziil* and *Tsosts'id ts'áadah* targets, with 19% and 18% of absorption relative to the continuum respectively.

VIS spectra of the Máaz formation targets tend toward greater 0.545 μm band depths and weaker 0.75–0.84 μm spectral slopes than those from the Séítah targets, although there is substantial overlap (Figures 5a and 5b). This results from the combined effects of overall greater contributions from ferric surfaces (dust, coatings) and no olivine in the Máaz targets.

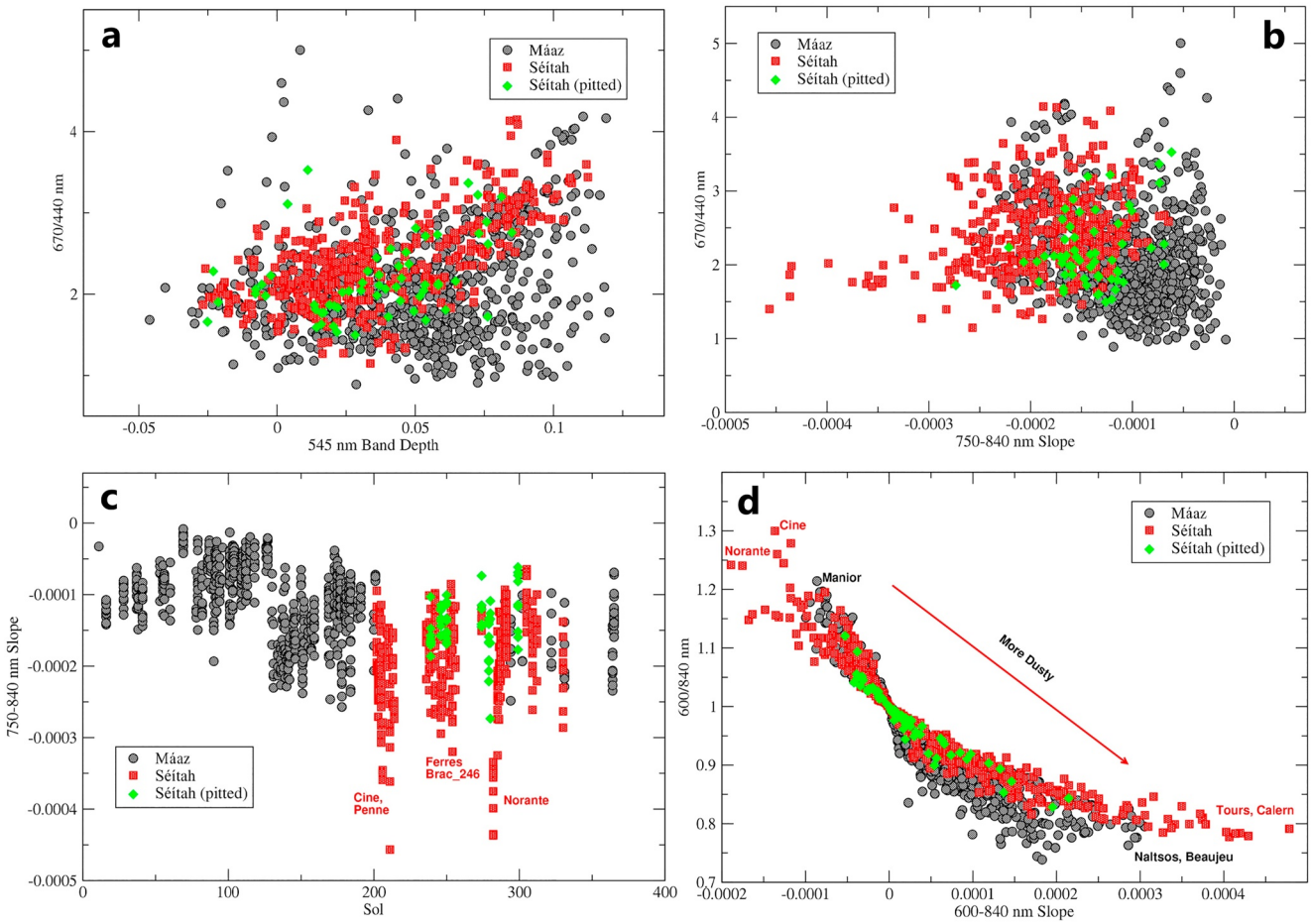

Figure 5. Visible wavelength spectral parameters for the Máaz, Séítah non-pitted, and Séítah pitted rock types. (a) 0.67/0.44 μm ratio ("redness") as a function of the 0.545 μm band depth (crystalline ferric materials). (b) 0.67/0.44 μm ratio as a function of the 0.75–0.84 μm spectral slope (mafic minerals and other Fe-bearing phases). (c) Variations in the 0.75–0.84 μm spectral slope as a function of sol number, demonstrating the onset of strong negative slopes related to the presence of olivine as the rover entered the Séítah region on sol 201. (d) 0.60/0.84 μm ratio as a function of the 0.60–0.84 μm spectral slope (dusty surfaces), which can serve as a proxy for dust coatings on spectrally neutral, low-albedo substrates (Johnson et al., 2015).

4.2.1. Phyllosilicates

Dark-toned rocks usually exhibit an absorption at 2.28 μm attributed to the Fe^{3+}–OH bond (40% of the individual point spectra, with a threshold of 1% absorption minimum; Figure 7). This band is often paired with additional absorptions at 1.42 μm (OH, H_2O) and 2.39 μm (Fe/Mg–OH) and is stronger when the water band is positioned at the lowest of the band range, at ∼1.92 μm (Figures 6 and 7). These observations indicate the presence of an Fe^{3+}-phyllosilicate such as nontronite or hisingerite, best expressed in the spectra of the *Bidziil* target (Figure 6b), a vertical facet of a rock (and hence a relatively dust-free target). While nontronite and hisingerite can form in different settings, these two species have similar spectral features and are hardly distinguishable in the VISIR spectral range (Milliken & Bish, 2014). Pure nontronite or hisingerite should have a 1.9 μm absorption band centered at shorter wavelength (∼1.91 μm) and with a narrower shape, indicating that this band is likely induced by the mixture of different hydrated minerals. An additional faint absorption was observed at 2.32–2.33 μm (Figure 3), suggesting that a slight amount of some Mg–OH mineral(s) (such as Mg-phyllosilicates and/or brucite) or carbonate might be occurring in mixture with the Fe-phyllosilicates or that an Fe/Mg-OH phyllosilicate is present.

4.2.2. Oxyhydroxides

Overall, the 2.28 μm band indicative of Fe-phyllosilicates is relatively shallow, exceeding 3% of absorption relative to the continuum in only 5% of the single-point spectra on the dark-toned rocks. Additionally, no clear

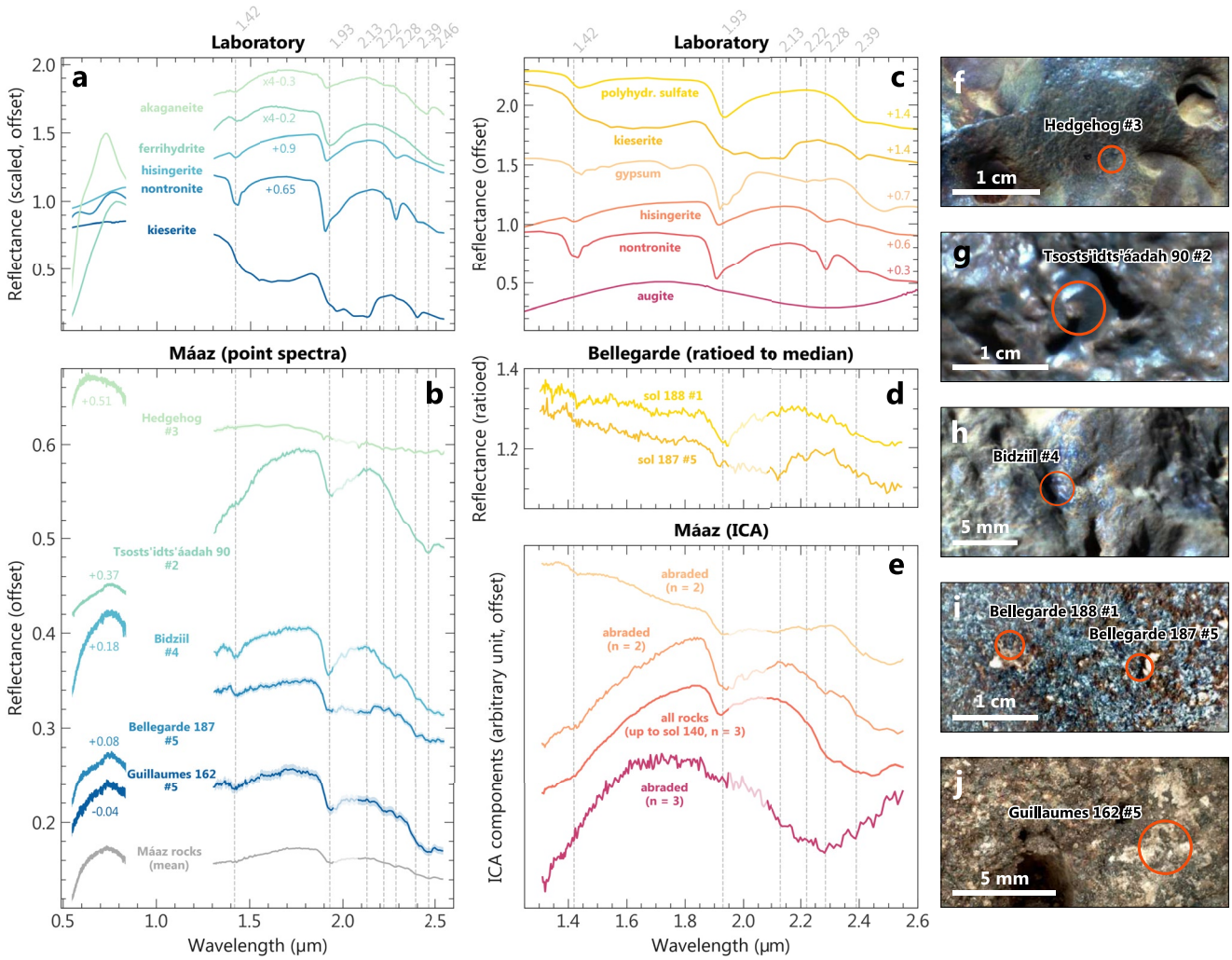

Figure 6. Spectral endmembers of the Máaz formation rocks. (a) Laboratory spectra from the RELAB spectral library (kieserite F1CC15, nontronite CBJB26, hisingerite C1RM137, ferrihydrite C1JB45, and akaganeite C1JB48). (b) Mean spectra of endmember rock targets within the Máaz formation as well as single-point spectra showing similar spectral features as the library spectra displayed in panel (a). Segments of the spectra shown with lower opacity line near 2 μm correspond to the main atmospheric CO_2 absorption domain, where residuals might affect the spectra. (c) Laboratory spectra from the RELAB spectral library (augite C1SC35, nontronite CBJB26, hisingerite C1RM137, gypsum BKR1JB556, kieserite F1CC15, and polyhydrated sulfate 799F366). (d) Point spectra on the abraded patch *Bellegarde* ratioed to the raster's median and showing similar spectral features as the Mg-sulfates spectra showed in panel (c), including a large absorption near 2.13 μm. The sol 188 ratioed spectrum has absorptions and spectral shape similar to polyhydrated sulfates; other hydrated minerals such as zeolites can also exhibit the same spectra but are less favored by laser-induced breakdown spectroscopy analysis (Meslin et al., 2022). (e) Independent Component Analysis loadings showing near-infrared spectral features similar to the spectra displayed in (c), with *n* the number of components in input. (f–i) Contrast-enhanced Remote Micro-Imaging close-ups on the holey rock *Hedgehog* (f), on a dark filled void of target *Tsosts'id ts'áadah* (g), on target *Bidziil* (h), and on the abraded patch *Bellegarde* (i). (j) Wide Angle Topographic Sensor for Operations and eNgineering close-up on the abraded patch *Guillaumes*. Red circles indicate the location of the field of view of the infrared spectrometer accounting for 68% of signal. See Text S1 in Supporting Information S1 for image IDs.

correlation between the 1.9 and 2.28 μm band depths was observed (Figure 7c). These observations along with the large range of 1.9 μm H_2O band positions point toward the presence of at least another hydrated mineral phase in the Máaz formation. Indeed, in some spectra, the 1.42, 2.28, and 2.39 μm bands are weak or nonexistent and are associated with a strong and wider water band centered at ~1.94 μm (Figure 6b). These features are consistent with a mixing with an Fe-oxyhydroxide, such as ferrihydrite. The best example was found on sol 90 in a dark-toned filled-vesicle of the *Tsosts'id ts'áadah* target mentioned above (Figure 6). This is in agreement with the LIBS coanalysis, which revealed ~80% FeOT in this target, consistent with the presence of Fe-oxyhydroxides (Clavé et al., 2022; Wiens et al., 2022). In the spectra of *Tsosts'id ts'áadah*, an additional absorption near 2.46 μm suggests that akaganeite (an Fe/Cl-oxyhydroxide) might be present as well. The laboratory spectra of other minerals such as some serpentines, brucite, carbonates, illite, or muscovite can exhibit a 2.46 μm absorption, but

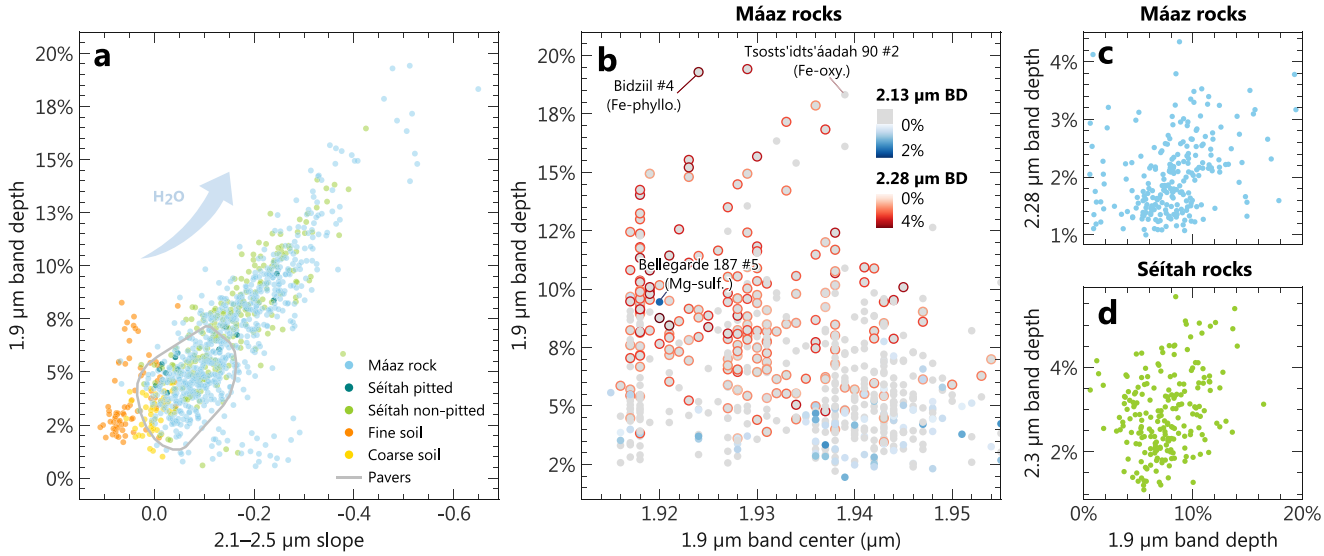

Figure 7. (a) Spectral parameters tracking the hydration signature in the near-infrared spectra. The pavers' distribution is delimited by the kernel density estimate of the points with an isoproportion level set at 75%. (b) Intensity of the 1.9 µm water absorption as a function of its position, color-coded with the intensity of the 2.28 µm (Fe^{3+}–OH) and 2.13 µm (Mg-sulfate) absorptions (BD: Band Depth). Spectral endmembers identified in Figure 6b are reported in the plot. (c) Intensity of the 2.28 µm (Fe^{3+}–OH) absorption as a function of the 1.9 µm (water) band depth, showing poor correlation for the Máaz rocks spectra. (d) Intensity of the 2.3 µm absorption (Fe–OH, Mg–OH, and CO_3) as a function of the 1.9 µm (water) band depth, showing poor correlation for the Séítah rocks spectra. See Table 1 for the parameter definitions.

show additional bands in the 2.2–2.3 µm range that are not observed here (see Carter, Viviano-Beck, et al., 2015 for a review).

4.2.3. Sulfates

Additionally, some spectra exhibit a significant absorption related to water (1.9 µm band depth of ~10%), with a downturn longward of ~2.3 µm. This was especially observed in the spectra of abraded rocks (e.g., the *Bellegarde* and *Guillaumes* targets; Figure 6). In *Bellegarde*, spectra ratioed by the raster median have absorptions and overall spectral shape similar to those of polyhydrated sulfates (such as starkeyite, hexahydrite, and schwertmannite; Figure 6d). Though this spectral shape can also be explained by the presence of zeolite or other poorly crystalline minerals containing water, coanalysis with LIBS shows a stronger sulfate component in this target (Meslin et al., 2022). Single-point and ratioed spectra in *Bellegarde* also exhibit a 1.93–2.13 µm "box-shaped" absorption shouldered at ~1.8 and 2.2 µm with an absorption maximum near 2.13 µm (Figures 6b and 6d): this is usually observed in the spectra of monohydrated Mg/Fe-sulfates of the kieserite–szomolnokite solid solution (e.g., Figure 6c). The spectra of these species also exhibit a faint absorption near 2.4 µm, which is observed in the non-ratioed spectrum of *Bellegarde* shown in Figure 6, but not in the ratioed one. The 2.13 µm feature has also been reported for one hydrated perchlorate spectrum by Hanley et al. (2009), but the strength of this band is minor in the published literature (Bishop et al., 2014). Using LIBS and Raman data, Meslin et al. (2022) reported the presence of Mg-sulfates in Máaz abraded patches, but no Fe-sulfate, making the Mg-kieserite species more likely to explain the 2.13 µm band observed in the VISIR spectra. Overall, this 2.13 µm feature is not commonly observed in Máaz rocks spectra (see Section 5.2.1).

4.2.4. Other Mineral Phases

In some Máaz rocks, a faint absorption at ~2.2 µm was observed (e.g., the *Guillaumes* target; Figure 6b). This band can be caused by the presence of an Al-phyllosilicate, hydrated silica, or gypsum.

While most of the rock targets show some degrees of hydration, some smooth and pitted rocks such as the target *Hedgehog* are exceptions, with weak to nonexistent 1.9 µm absorptions, blue slopes, and subtle wide absorptions around ~1 µm (Figure 6). These relatively featureless spectra might indicate a low mafic minerals content, or result from small grain size. Some extremely high-Ca, low-Fe pyroxenes also exhibit similar spectral features with subdued absorption at 2 µm (Horgan et al., 2014; Figure 6). From LIBS data, these targets exhibit similar

elemental compositions compared to the surrounding rocks, suggesting no strongly variable composition (Udry et al., 2022).

4.2.5. Independent Component Analysis

In the ICA model considering $n = 3$ components mixed in the abraded rocks of the Máaz formation, *Guillaumes* and *Bellegarde*, one of the resulting components exhibits a red slope in the 1.3–1.7 μm range as well as a broad and large absorption centered at 2.3 μm, consistent with high-Ca pyroxene (Figure 6), also detected by the LIBS and PIXL instruments (Razzell Hollis et al., 2022; Wiens et al., 2022). In the $n = 2$ model run on these same targets, one of the resulting components shows a sharp downturn past 2.3 μm as well as absorptions at 1.43, 1.93 μm, and a very weak feature at 2.13 μm (Figure 6e), consistent with Mg-sulfates. The other component exhibits a large absorption at 1.94 μm (similar to those of the *Tsosts'id ts'áadah* spectrum), as well as shallow absorptions at 1.42, 2.28, and 2.39 μm (similar to those of the *Bidziil* spectrum). This component likely corresponds to an Fe-phyllosilicate and Fe-oxyhydroxide mixture. ICA analysis was also performed on all rock targets of the Máaz formation, considering $n = 3$ components. One of the corresponding component is similar to the possible Fe-oxyhydroxide and Fe-phyllosilicate mixture (Figure 6e).

4.3. Rocks of the Séítah Formation: Non-Pitted Rocks

4.3.1. Olivine

The VISIR single-point spectra of Séítah non-pitted rocks are significantly different from those measured in the Máaz formation, with a distinctly stronger absorption between ∼0.7 and ∼1.8 μm typical of olivine (with possible minor contributions from other Fe-rich minerals; Figures 3, 8 and 9a). The greater olivine contributions in many of the Séítah targets are expressed by the stronger negative 0.75–0.84 μm spectral slopes exemplified in Figure 5c (targets *Cine*, *Penne*), where the major spectral change occurred around sol 200 when Perseverance entered the Séítah region.

While exhibiting a strong absorption related to olivine, these spectra also show a negative 2.1–2.5 μm slope (Figure 10) as well as an absorption band of water near 1.9 μm (Figure 8), showing that hydrated products are widespread in the unit, similar to the Máaz formation rocks. The depth of this absorption is on the same order as for the Máaz rocks (Figures 3, 7a and 9b), with the strongest water band depth being observed at 16% and 14% absorption relative to the continuum (for the targets *Issole* and *Penne*, respectively).

4.3.2. Phyllosilicates and Carbonates

In most of the less dusty non-pitted rocks in Séítah, an absorption at ∼2.3 μm, whose shape and center exhibits significant variations, is observed. In some of these single-point spectra, a doublet of sharp bands showing minima centered at 2.28 and 2.32–2.33 μm, respectively (Figure 3c and *Dourbes* tailings in Figure 8), consistent with a mixture of Fe-phyllosilicates (such as nontronite or hisingerite) and some carbonates and/or Mg–OH mineral(s), respectively. The latter could be an Mg-phyllosilicate (such as a smectite, a serpentine or talc) or a magnesium hydroxide (such as brucite). Additional very shallow bands at ∼2.4 and 2.47 μm were observed (respectively, 1.2% and 0.7% of absorption relative to the continuum in the tailings of the *Dourbes* target; Figure 8). If real, they could suggest that talc may be a good candidate for the potential Mg–OH mineral (Figure 8a; Brown et al., 2022); however, the two bands are near detection limit. In some other spectra, the 2.3 μm band does not exhibit any doublet and instead shows a single, wider, and usually stronger absorption centered at 2.32 μm (Figures 8 and 9). While a 2.32 μm absorption was also observed in the Máaz rocks spectra, it is generally stronger in those of the Séítah rocks (Figure 9c).

No correlation between the 1.9 and 2.3 μm band depths was observed (Figure 7d), suggesting that the 1.9 μm band is explained by minerals with no Fe/Mg–OH bands (such as ferrihydrite), that the hydration of the metal-OH bearing phase itself is variable, which would not be unexpected for clay minerals (interlayers more or less collapsed), or that at least one nonhydrated mineral phase contributes to the absorption near 2.3 μm. In the *Garde* abraded patch, a shallow band at 2.53 μm is observed, together with an absorption at 2.32 μm (Figure 8e). This absorption near 2.5 μm can be due to the presence of carbonates, although some spectra of clay minerals (e.g., serpentine) can also exhibit this feature. On the target *Garde*, Clavé et al. (2022) reported one of the strongest signatures of carbonates of all the LIBS and Raman spectra measured on the crater floor. Hence, we favor the hypothesis that the absorption near 2.5 μm observed in this specific target is related to carbonates. Notably, this

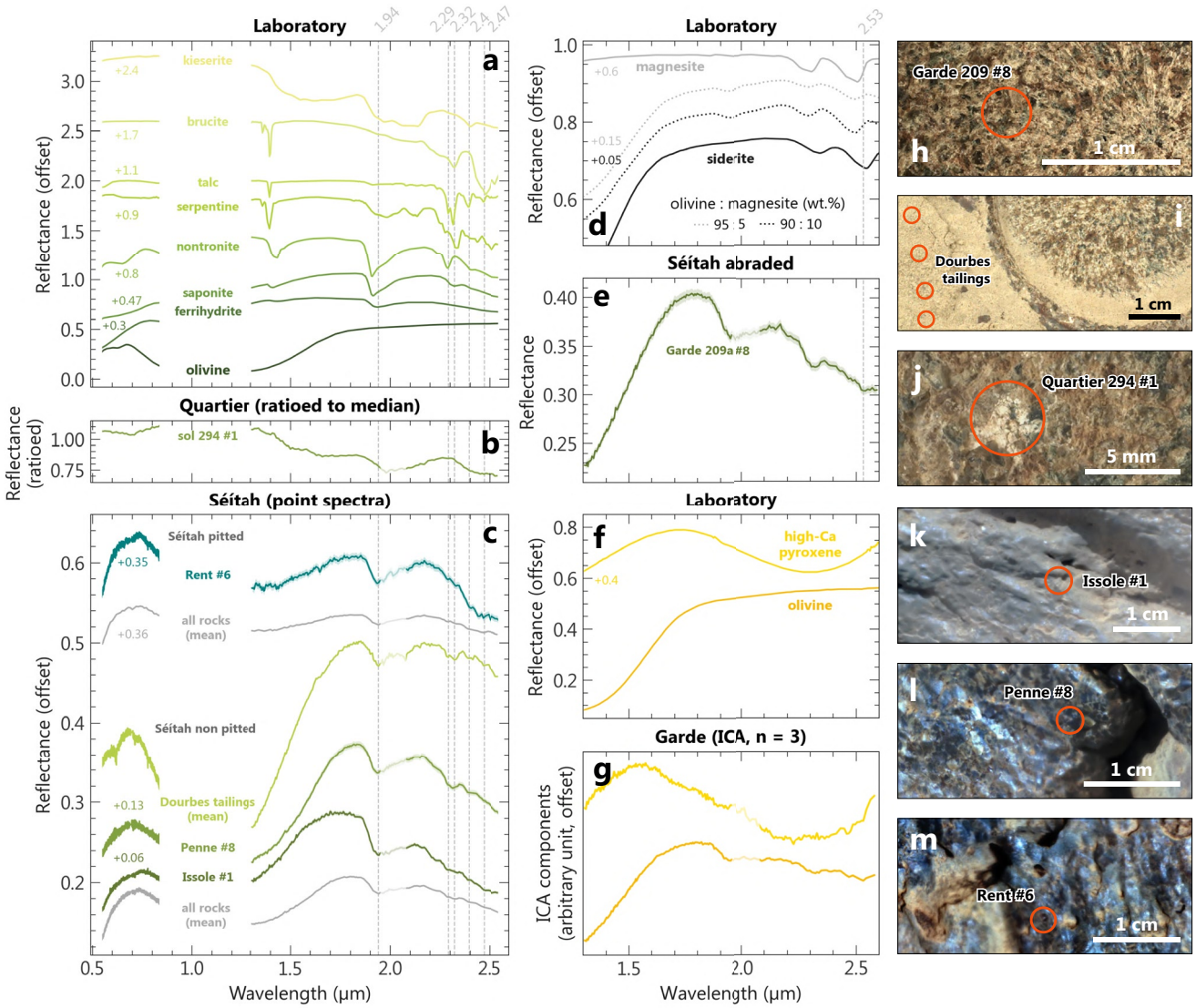

Figure 8. Spectral endmembers of the Séítah formation rocks. (a) Laboratory spectra from the RELAB library (olivine C1PO47, ferrihydrite C1JB45, saponite LASA59, nontronite CBJB26, serpentine LASR10, talc LAEA15, brucite C1JB944, and kieserite F1CC15). (b) Point spectrum on the abraded patch *Quartier* ratioed to the raster median and showing similar spectral features as the mono-hydrated Mg-sulfates spectrum of kieserite showed in panel (a). (c) Mean spectra of rock targets in the Séítah formation as well as individual point spectra showing similar spectral features as the library spectra displayed in panel (a). Segments of the spectra shown with lower opacity line near 2 µm correspond to the main atmospheric CO_2 absorption domain, where residuals might affect the spectra. (d) Laboratory spectra of olivine (grain size: 0.1–1 mm) and magnesite (<0.1 mm) compact mixtures (from Mandon et al., 2022) along with spectra from the RELAB library (magnesite KACB06A and siderite LACB08A). (e) Point spectrum on the abraded patch *Garde*, in which carbonates were detected by laser-induced breakdown spectroscopy and Raman (Clavé et al., 2022). Note the presence of a band near 2.5 µm, possibly explained by a small contribution from carbonates. (f) Laboratory spectra from the RELAB library (olivine C1PO47 Fo_{50-70}, undefined grainsize; pyroxene C1SC35, augite, 45–90 µm particulate). (g) Independent Component Analysis loadings showing near-infrared spectral features similar to the spectra displayed in panels (d and f), with three components in input. (h–j) Wide Angle Topographic Sensor for Operations and eNgineering close-ups on the abraded patches *Garde*, *Dourbes,* and *Quartier*. (k–m) Contrast-enhanced Remote Micro-Imaging close-ups on the rock targets *Issole*, *Penne* (non-pitted), and *Rent* (pitted). Red circles indicate the location of the field of view of the infrared spectrometer accounting for 68% of signal. See Text S1 in Supporting Information S1 for image IDs.

band is weaker than the 2.3 µm band, whereas the opposite would be expected if it were solely due to carbonate. As such, it likely represents a mixture of carbonates with Fe/Mg-phyllosilicates (which also contribute to the 2.3 µm absorption). Once the continuum is removed, the 2.3 and 2.5 µm bands observed in the *Garde* target are centered at 2.31 and 2.53 µm, respectively. This is in agreement with bands associated with Fe/Mg-carbonates, and consistent with the composition inferred from LIBS data (Clavé et al., 2022) and from orbit at the regional scale (Ehlmann et al., 2008).

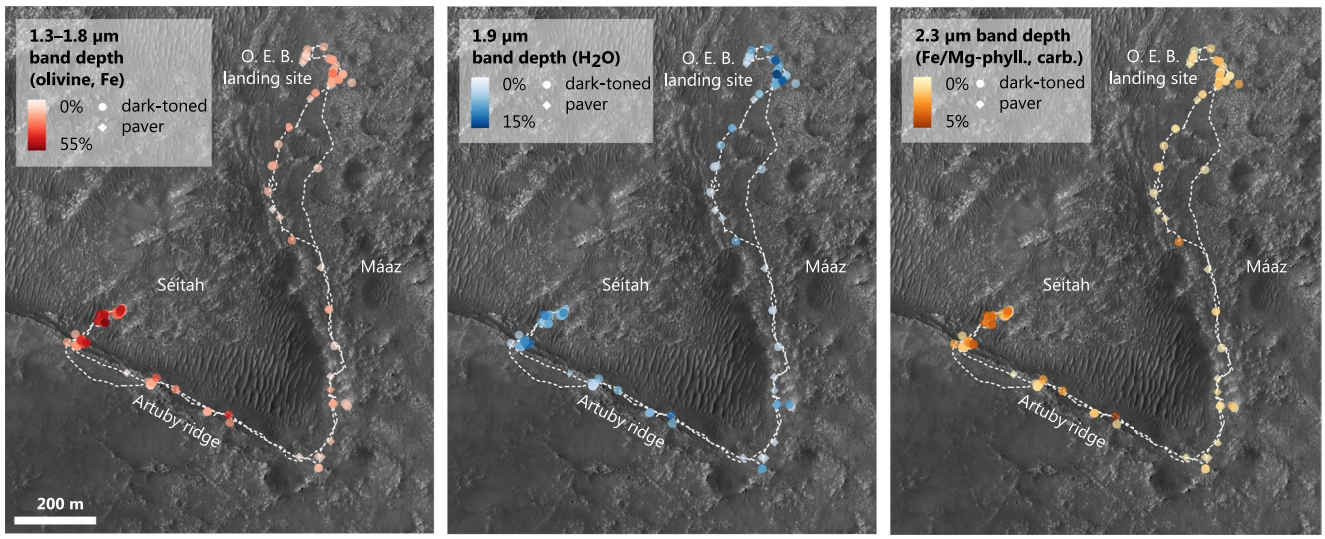

Figure 9. Spectral parameter maps along the rover traverse, up to sol 379 overlain on a High Resolution Imaging Science Experiment mosaic (Fergason et al., 2020; McEwen et al., 2007). The Séítah formation is generally outcropping at higher elevation than the Máaz formation but is stratigraphically on a lowest level (Farley et al., 2022; Wiens et al., 2022).

Given the implication of observing an absorption near 2.5 µm, its significance was investigated in more detail in the companion paper by Royer et al. (2022): in the *Garde* spectra, the absorption at 2.53 µm is observed at band SNR >3 in 5 single-point spectra out of 27 (SNR = 1 being the band detection threshold, as the signal is equal to the estimated noise). In particular, the *Garde* sol 209 #8 spectrum exhibits an absorption at 2.53 µm at a band SNR of 7, which indicates that it is likely not induced by instrumental effects.

By comparison with the spectra of mixtures of carbonate and olivine, the carbonate proportion in the field of view of the IRS is likely minor. Indeed, as shown in Figures 8d and 8e, the relative band depths at 2.5 µm (carbonate) and 1.3 µm (olivine) in the *Garde* spectrum are weaker than in the 95 wt.% olivine and 5 wt.% carbonate mixture spectrum measured by Mandon et al. (2022). Analysis of the SCCTs has shown overall weaker contrast and band depth on the IRS spectra measured on Mars compared to laboratory measurements (Royer et al., 2022), and grain size and complex mixture can greatly affect the depth of the absorption bands (e.g., Crowley, 1986; Zaini et al., 2012), so great care should be taken when comparing to laboratory measurements of mixtures. Still, observations of a band near 2.5 µm are very scarce in the spectral data set of the crater floor and observed at maximum 3%–4% band depth which is very weak. This is in agreement with the low proportion of carbonates in the Séítah rocks inferred by Clavé et al. (2022).

On the orbital data, the southern part of Séítah exhibits relatively weak carbonate signature, which is in agreement with the scarce observations of the absorption near 2.5 µm (Horgan et al., 2020; Figure S3b in Supporting Information S1). After the first campaign of Mars 2020 and before reaching the base of the deltaic deposits, Perseverance explored the western region of Séítah, which from orbit shows stronger carbonate signatures. Consistently, VISIR reflectance spectra of the rocks at this location exhibit distinct bands at 2.53 µm, similar to the *Garde* observation (Figure S3a in Supporting Information S1).

4.3.3. Oxyhydroxides

In *Issole*, a non-pitted rock, a strong (16% of absorption relative to the continuum) and large hydration band at ~1.9 µm was observed, as well as subdued bands in the metal–OH absorptions region, in addition to the olivine absorption typical of the Séítah rocks (Figure 8c). Apart from the olivine absorption, these spectral features are similar to those observed in the spectrum of *Tsosts'id ts'áadah*, interpreted as Fe-oxyhydroxide-bearing. As such, this type of minerals might be common to the Séítah and Máaz formations. Still, these spectral features are overall rarely observed in the Séítah rocks spectra.

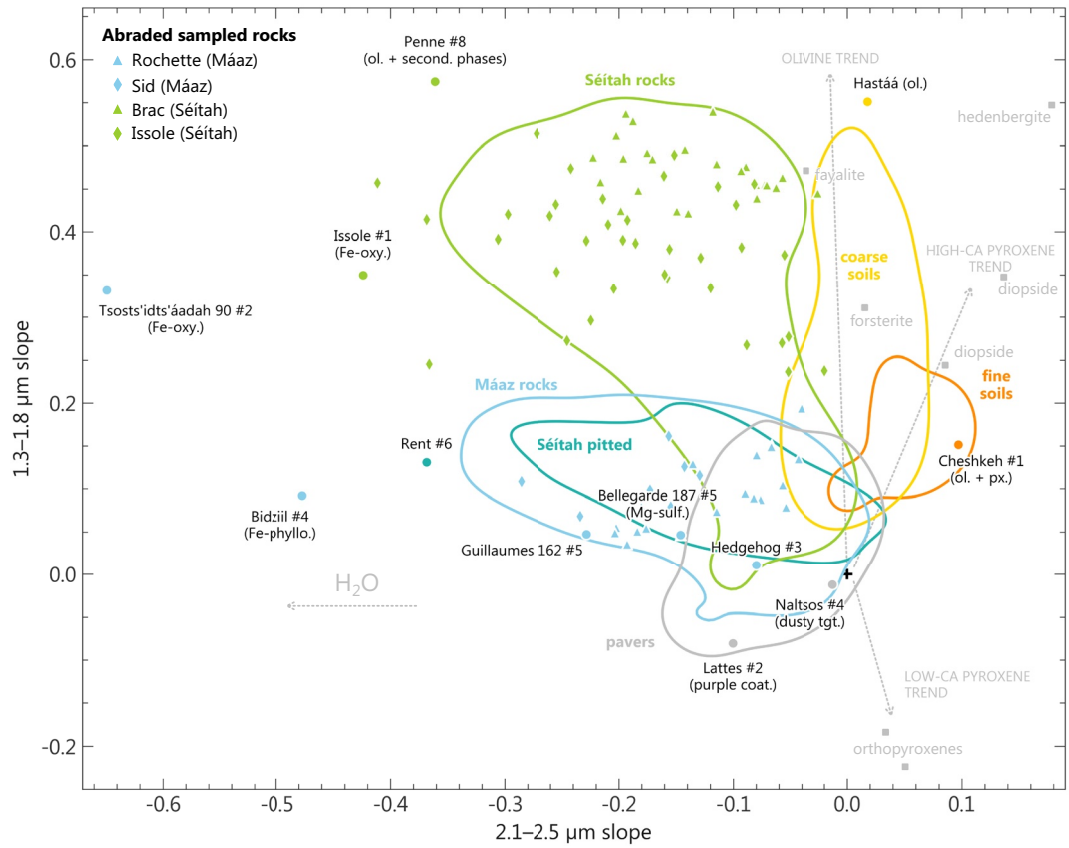

Figure 10. Diversity of the spectral shapes in the near-infrared for all the point spectra measured on the crater floor (solid lines), point spectra endmembers shown in previous figures (circle points), and sampled rocks (triangles and diamonds points). Solid lines delimit the kernel density estimate of the distributions for each type of observations, with an iso-proportion level set at 75%. Dotted lines indicate the trend of various mineral families inferred from laboratory spectra from the RELAB library (olivines and pyroxenes in gray squares). Pavers (dustiest rocks) include both targets from the Máaz and Séítah formations. The reader is referred to Section 3.4.3 and Table 1 for the definition and sensitivity of the 1.3–1.8 and 2.1–2.5 µm slope parameters.

4.3.4. Other Mineral Phases

In the abraded patch *Quartier*, some light-toned areas were observed, similarly to the *Bellegarde* and *Guillaumes* patches in the Máaz formation. One of these light-toned features was largely included in the field of view of some SuperCam VISIR measurements (Figure 8j); ratioing the corresponding spectrum by the raster median highlighted spectral features similar to those in the *Bellegarde* target that were interpreted to be due to the possible presence of sulfate and/or poorly crystalline water-bearing materials (Figure 8b).

Finally, an absorption shoulder was observed in the spectra of the Séítah rocks at 2.22–2.23 µm (Figure 3). This can be induced by both Al–OH mineral phase(s) or hydrated silica. In LIBS data, several points high in silica have been observed and are unlikely to correspond to quartz in a mafic rock consisting of ∼40% olivine (Wiens et al., 2022), and might be related to potential secondary hydrated silica (e.g., opal or chalcedony), causing the absorption at 2.2 µm. Given the weak absorption associated with this band, both Al–OH phases and hydrated silica remain a possibility to explain its occurrence in Séítah rocks.

4.3.5. Independent Component Analysis

Similarly to the Máaz rocks, one of the ICA components of the abraded rocks NIR spectra in Séítah shows a red slope in the 1.3–1.6 µm range, as well as a broad and large absorption centered at 2.3 µm, consistent with high-Ca pyroxene (Figure 8). Another component exhibits spectral features similar to olivine mixed with carbonates and/or Fe/Mg-phyllosilicates. The ICA models run on the spectra of the Séítah rocks have not yet been able to distinguish olivine from secondary minerals products, and while an unaltered pyroxene component could be retrieved,

no pristine olivine component was observed. This might suggest that the proportion of the alteration products varies as the olivine proportion does and that they are preferentially spatially associated with olivine compared to pyroxene, at the scale of the IRS field of view (e.g., in cracks or on the rims of the olivine crystals). This is consistent with olivine usually altering more rapidly than pyroxene.

4.4. Rocks of the Séítah Formation: Pitted Rocks

In total, seven different pitted rocks (the rocks near the top of the stratigraphy of Séítah) have been measured in the VISIR by SuperCam. Unlike the other rocks in Séítah, their single-point spectra do not exhibit the wide absorption between ∼0.7 and ∼1.8 μm typical of olivine but rather exhibit spectral shape similar to those of the Máaz rocks in the overall VISIR range (Figure 8c). In particular, the spectral slopes in the 0.75–0.84, 1.3–1.8, and 2.1–2.5 μm ranges are on the same order than the spectra measured on the Máaz rocks (Figures 5 and 10). The lack of absorption indicative of olivine is in agreement with the Mg-poor and olivine-lacking composition inferred from LIBS data on these pitted rocks (Wiens et al., 2022).

4.5. Soils

During the crater floor campaign, different types of regolith were observed (Cousin, Meslin, et al., 2022; Vaughan et al., 2021). In particular, we distinguish fine soils, which are associated with μm-scale particles coated with dust (Hausrath et al., 2022), and coarse soils, which consist of an assemblage of fine and coarser mm-sized materials. On the crater floor, the latter is usually found on eolian bedforms and much of the coarser fraction consists of dark-toned mm-sized granules (Figure 11). In the VISIR data, both types of soils have distinct spectral signatures in the near-infrared. The spectra of fine soils, such as the *Cheshkeh* target, exhibit two large absorptions in the ∼0.7–1.7 and ∼1.7–2.4 μm ranges, consistent with pyroxene, possibly mixed with olivine (Figure 11 and Figure S4 in Supporting Information S1). The second absorption is broadly centered around 2.0–2.1 μm, corresponding to pyroxene of intermediate composition—either resulting from the mixing of pyroxenes of different Ca-composition or from a unique type of pyroxene with intermediate Ca content. The spectra measured on the coarse-grained soils, such as the *Hastaa* sand ripple target, show a deeper absorption between ∼0.7 and 1.7 μm and do not exhibit the 2.0–2.1 μm broad band observed in the soils spectra (Figure 11). This is consistent with a significant enrichment in olivine compared to the fine soils (though grain size and Fo content influence the olivine signature as well), in agreement with the higher content of Mg and the stoichiometry consistent with almost pure olivine inferred from LIBS data on these dark-toned grains (Cousin, Meslin, et al., 2022). This variability in composition is easily observed in Figure 10, where the coarse soils plot along the olivine trend in the spectral slopes parameter space and the finer soils plot between the olivine and pyroxene trends.

Fine and coarse soils share overall similar spectral shapes whether observed on the Máaz or Séítah formations (Figure S4 in Supporting Information S1). Slight differences were observed: in the fine soils spectra, the 2.1–2.5 μm slope is of 4% on average for both formation, while the 1.3–1.8 μm slope is of 16% and 22% on average on the Máaz and Séítah formation, respectively. The latter suggests slightly more mafic minerals in the fine soils of the Séítah formation. In line with this, coarse soils exhibit a 1.3–1.8 μm slope of 25% and 32% on average on the Máaz and Séítah formation, respectively. The 2.1–2.5 μm slope is similar for both types of coarse soils, with 0.5% and 1% on average for Máaz and Séítah.

The spectra measured by the IRS on the soils commonly exhibit a shallow absorption related to hydration at ∼1.9 μm. This band was observed at similar strength for both types of soils, at 4% and 3% absorption relative to the continuum for the fine and coarse soils, respectively (Figure 7a). These values are significantly lower than in the observations of rocks, which, for dark-toned (i.e., less dusty targets) is of 8% relative to the continuum. In the spectra of coarse soils, additional absorptions at 2.28 and 2.32 μm, or 2.30 μm were observed, attributed to a combination of Fe–OH and Mg–OH phases (Figure 11 and Figure S4 in Supporting Information S1). The large absorption in the ∼0.7–1.7 μm range induced by olivine and these two shallow bands around 2.3 μm observed in coarse soils in both two units of the crater floor are spectral characteristics shared with the spectra measured on the non-pitted rocks of the Séítah formation, implying a common composition between the dark-toned granules in the soils and the Séítah rocks.

ICA analysis of the regolith spectra confirms the results above and highlights the three following components for the soils (in no preferential order): a first component consistent with intermediate-Ca pyroxene or a mixture

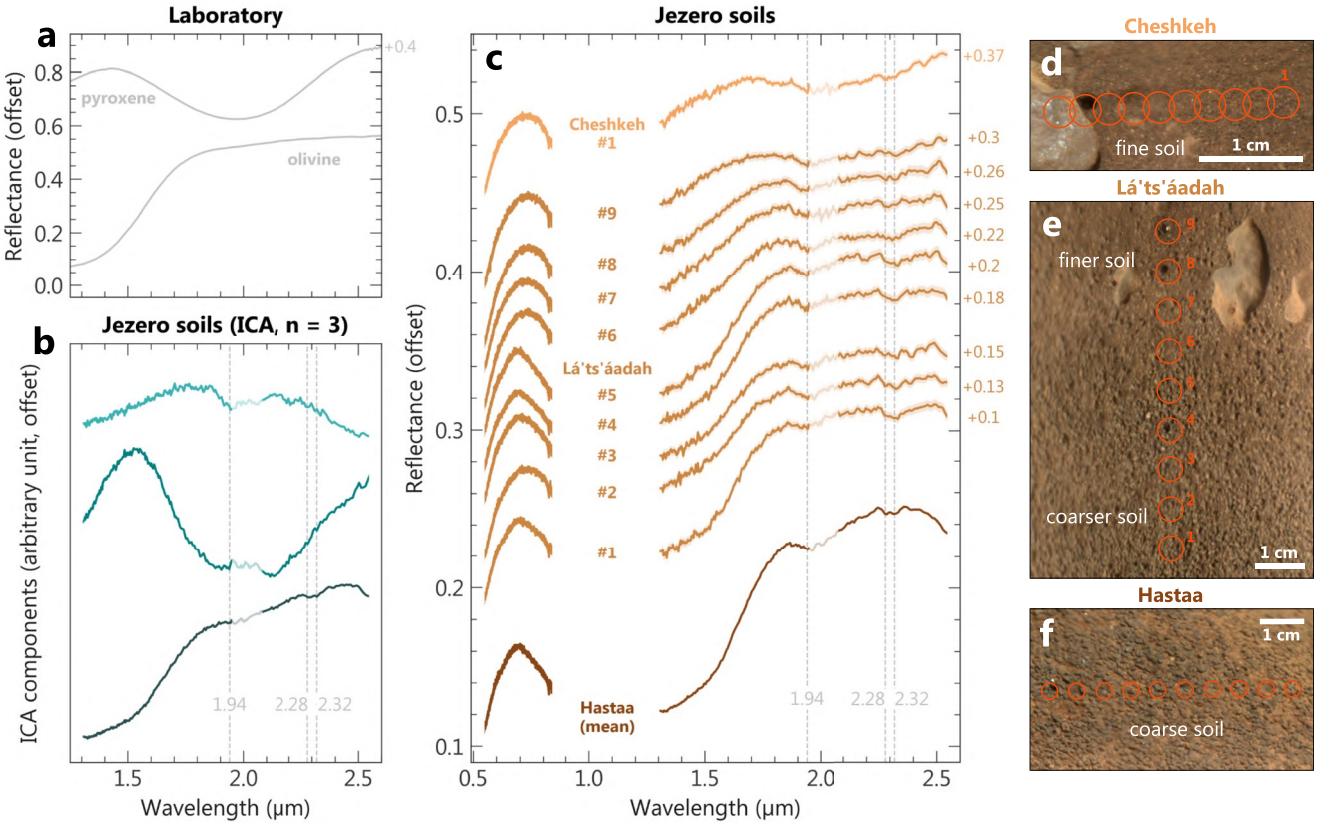

Figure 11. Spectral signature of the Máaz formation regolith. (a) Laboratory spectra from the RELAB spectral library (olivine C1PO47 Fo_{50-70}, undefined grainsize; pyroxene C1SC35, augite, 45–90 μm particulate). (b) Results of the Independent Component Analysis considering three individual components. (c) Point spectra of selected regolith observations in the Máaz formation along with the corresponding Remote Micro-Imaging images in panels (d–f). Segments of the spectra shown with lower opacity line near 2 μm correspond to the main atmospheric CO_2 absorption domain, where residuals might affect the spectra. Red circles indicate the location of the field of view of the infrared spectrometer accounting for 68% of signal. The *Cheshkeh* target, observed on sol 116, is a fine soil with micrometer-sized particles, while the *Hastaa* target, observed on sol 106 is coarse-grained, with millimeter-sized granules. *Lá'ts'áadah* was observed on sol 110 and exhibits a transition of granulometry within the raster, from millimeter-sized granules to micrometer-sized particles, correlated with an increase of the olivine absorption. See Text S1 in Supporting Information S1 for image IDs.

of various pyroxene types of distinct composition (broad absorption centered at ~2 μm); a second component consistent with olivine mixed with carbonates and/or Fe/Mg-phyllosilicates (large absorption in the 1.3–1.8 μm range and shallow absorptions centered in the 2.28–2.32 μm range), which is similar to Séítah rocks; and a third component corresponding to some hydration of uncertain nature (single absorption at 1.94 μm; Figure 11).

While the coarser soils share spectral similarities with the Séítah rocks (a wide 0.7–1.8 μm absorption, shallower ~1.9 and 2.3 μm absorptions), their 2.1–2.5 μm slope is weaker (Figure 10). This might be explained by the presence of finer, pyroxene-rich soils in the field of view of the IRS or by a weaker water content in the coarse soils compared to Séítah rocks, consistent with their weaker 1.9 μm band.

4.6. Cached Samples

We report in Figure 12 the spectra of the different targets related to the sampled rocks: natural and abraded surfaces of the sampled rocks and tailings resulting from their coring or abrasion. The corresponding spectra are compared to the mean spectra of each of the geologic unit the samples are related to, as a means to estimate their representativeness. During the crater floor campaign, eight rock cores were collected and sealed, comprising two paired samples at each of the following outcrops: *Rochette* and *Sid* in the flat-lower and massive-upper Máaz formation, respectively, and *Brac* and *Issole* in the Séítah formation (Figure 1, see Text S2 in Supporting Information S1 for the list of target names). No sample was acquired from the pitted rocks of the Séítah unit.

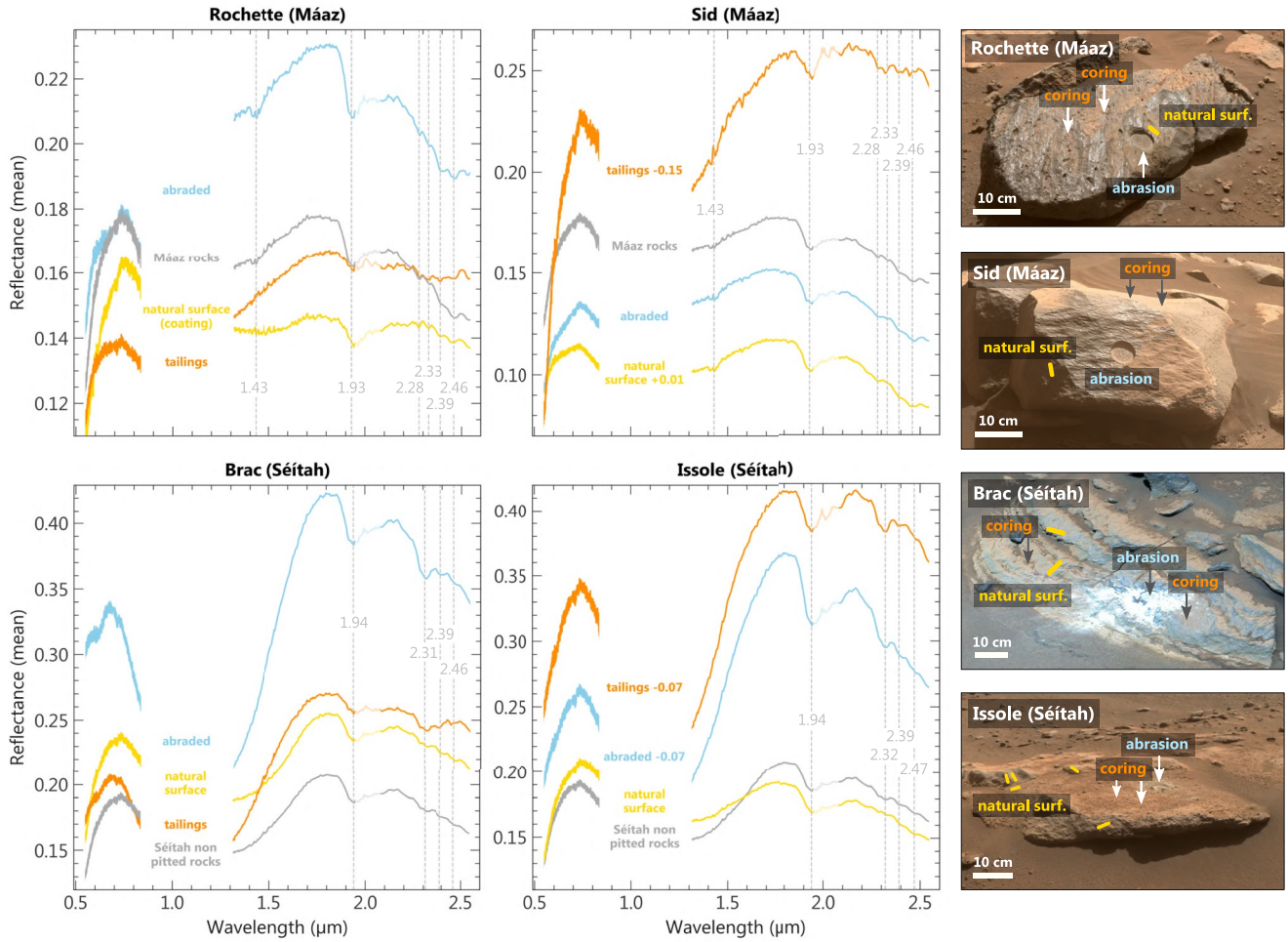

Figure 12. Visible and near-infrared (VSIR) spectra of the rocks sampled by Perseverance on the crater floor of Jezero along with Hazcams and Mastcam-Z context images. For each rock/outcrop (*Rochette*, *Sid*, *Brac*, and *Issole*), two samples were collected, and SuperCam measurements were performed on the natural and abraded surfaces, as well as on the tailings resulting from coring or abrasion activities. See Text S2 in Supporting Information S1 for the list of targets considered in the averaged spectra. The positions of the main (possibly weak) absorptions identified to be recurring in the observations and meaningful for mineralogical interpretation are shown as vertical lines. Segments of the spectra shown with lower opacity line near 2 μm correspond to the main atmospheric CO_2 absorption domain, where residuals might affect the spectra. Note that these measurements were performed under variable phase angle, possibly affecting the absolute reflectance and spectral slopes. Yellow areas correspond to the locations of VISIR rasters performed on natural (i.e., non-abraded) surfaces. See Text S1 in Supporting Information S1 for image IDs.

After a coring activity, no measurement was performed by the science payload on the collected sample. SuperCam analyses were performed on the boreholes of the drills, but these targets were usually not sunlit, which complicates the interpretation of reflectance spectra. The abraded surfaces of the rock sampled on the crater floor are the freshest surfaces measured by SuperCam and the more likely to represent the lithologies of the sealed cores. These abraded targets have usually stronger absorptions than the natural rocks (Figure 12), which is expected given their low to absent dust cover and/or coatings.

The abraded *Rochette* and *Sid* outcrops have mean VISIR spectra similar to the mean signature of the Máaz rocks: they share a comparable overall spectral shape in the 0.5–2.5 μm range, including similar 0.545 μm band depths and 0.75–0.84 μm spectral slopes. In the near-infrared, they exhibit similar absorptions at 1.43, 1.93, 2.28, 2.39, and 2.46 μm (Figure 12). This indicates that the samples collected at *Rochette* and *Sid* are overall representative of the Máaz formation in terms of the alteration minerals assemblage present in the rocks. These two Máaz abraded rocks are similar in terms of the spectral intensity of the 1.9 μm water absorption (8% average, relative to the continuum) as well as the 2.28 μm Fe-phyllosilicate band (1.5% average).

The abraded *Brac* and *Issole* outcrops are representative of the Séítah formation as well, and exhibit similar spectra compared to the rocks measured in this unit: negative 0.545 μm band depths, but strong absorption between

0.7 and 1.8 μm consistent with the presence of olivine, possibly mixed with other ferrous components. They also exhibit absorption bands at 1.94, 2.3, 2.39, and 2.46 μm related to the secondary mineral phases discussed previously for Séítah rocks. Both abraded rocks have similar 1.3–1.8 μm olivine/ferrous mineral band depth (45% average relative to the continuum at 1.3 μm) and Fe/Mg-phyllosilicate and/or carbonate 2.3 μm band depth (5% average). The 1.9 μm water band is slightly stronger at *Issole* compared to *Brac* (11% and 8% average, respectively).

Interestingly, at *Rochette* and *Sid*, the abraded rock and tailings spectra exhibit significantly different spectral signatures in the infrared. While strong H_2O and metal–OH bands were observed in the abraded spectra, similarly to other Máaz rocks, their tailings exhibit flatter spectra, along with subdued absorption bands (Figure 12). Potential interpretations of this phenomenon are provided in the discussion section.

5. Discussion

5.1. Igneous Nature of the Crater Floor

The VISIR spectra measured during the first year of the mission are in agreement with parallel studies proposing that the crater floor consists of igneous rocks, with altered basaltic rocks on top of the stratigraphy and olivine-rich rocks at the bottom (Beyssac et al., 2021; Farley et al., 2022; Liu, Tice, et al., 2022; Udry et al., 2022; Wiens et al., 2022).

5.1.1. The Máaz Formation

In the Máaz formation (east of the Séítah region, Artuby excluded), Wiens et al. (2022) reported basaltic compositions with mineral abundances (derived from LIBS CIPW norms and alteration phases excluded) of ∼45% feldspar and ∼43% pyroxene (mostly as Fe-rich augite and pigeonite; Udry et al., 2022). Oxides might also be present in the Máaz rocks. Fe-poor feldspars do not exhibit strong distinct absorption bands in the spectral range covered by SuperCam, making pyroxene the main primary mineral detectable in VISIR in the Máaz formation. Depending on grain size, hydrated minerals can have low detection thresholds in reflectance spectroscopy compared to mafic minerals (e.g., Mandon et al., 2022; Thollot, 2013), likely explaining the dominance of their signature in the Máaz rocks spectra. Still, our ICA analysis suggests the presence of high-Ca pyroxene in some targets, in agreement with the LIBS-derived compositions (Udry et al., 2022). No evidence of low-Ca pyroxene was observed based on the analysis of the VISIR spectra.

In orbital data over Jezero's delta and watershed, the signatures of low-Ca pyroxene, as well as olivine and carbonate are significant (Horgan et al., 2020). The fact that the corresponding signatures were not observed in the Máaz formation rocks strengthens the hypothesis favored by Farley et al. (2022), Wiens et al. (2022), and Udry et al. (2022) that this unit is not composed of igneous materials transported from the watershed but instead emplaced in situ through igneous processes (such as lava flows or pyroclastic deposits).

5.1.2. The Séítah Formation

Similarly to Máaz, the mineralogical assemblage observed in VISIR in the Séítah rocks does not include the low-Ca pyroxene signature observed on the watershed and on the delta, possibly favoring again the in situ magmatic/volcanic emplacement over the sedimentary hypothesis, consistent with Liu, Tice, et al. (2022).

Consistent with Wiens et al. (2022), no olivine was detected with the VISIR technique in the Séítah pitted rocks or in the Máaz formation, but it was detected in all the spectra of the Séítah non-pitted rocks. Farley et al. (2022) and Wiens et al. (2022) proposed various scenarios to explain this change of mineralogy between Máaz and Séítah, accounting for the cumulate texture of olivine-bearing rocks described by Liu, Tice, et al. (2022). In the first scenario, the terrains observed by Perseverance on the crater floor were formed after the differentiation of a single melt by gravity settling of olivine crystals (Brown et al., 2022). Alternatively, the Máaz formation (and possibly Artuby) could have formed from consecutive lava flows, after emplacement and erosion of the cumulate filling the crater floor. In these hypotheses, the origin of the cumulate formation is unclear and could result from the differentiation of an intrusive or thick extrusive igneous flow, or from an impact melt. Layers observed from orbital data in the regional Nili Fossae olivine-bearing unit drape the eroded rim of Jezero North to the delta, discarding an intrusive origin or a formation related to the older giant impact of Isidis (Mandon et al., 2020). Hence, if the Séítah formation exposes rocks of the regional olivine-bearing unit, an effusive scenario would be

favored. Until further exploration outside of Jezero crater, the clarification of the relationship between the rocks exposed at Jezero and the regional olivine-bearing unit, as well as its exact origin, remain to be determined.

5.2. Alteration of the Crater Floor

5.2.1. Nature of the Hydration

From orbital data, the crater floor of Jezero appears poorly hydrated, with primary mafic minerals dominating the CRISM spectra measured on Máaz and Séítah (e.g., Goudge et al., 2015; Horgan et al., 2020). Surprisingly, most of the SuperCam reflectance spectra of the rocks of the crater floor exhibit an absorption near 1.9 μm, related to water. Figures 7 and 9 show that the depth of the 1.9 μm band has comparable strength in the spectra of the Séítah and the Máaz rocks (slightly more intense in Máaz), pointing to roughly similar hydration levels in both formations. Pavers exhibit shallower hydration bands than massive dark-toned rocks, likely owing to their substantial dust cover which was often not completely removed within the VISIR fields of view by LIBS bursts prior to acquisition, and/or more adherent coatings. Abraded rocks of the upper part of the Máaz stratigraphy (*Alfalfa* target within the *Sid* sample site) and of the lower Máaz stratigraphy (*Guillaumes* and *Bellegarde* targets within the *Roubion* and *Rochette* sample sites, respectively) exhibit comparable average 1.9 μm absorption depths: 8% for the *Alfalfa* and *Bellegarde* targets and 11% for the *Guillaumes* target. This suggests overall similar hydrated mineral phases content throughout the Máaz stratigraphic column.

Several hydrated minerals that might cause the 1.9 μm absorption have been identified using VISIR data: Fe-oxyhydroxides, phyllosilicates, sulfates, and, if hydrated, carbonates (see Section 4). In reflectance spectroscopy, the strength of the absorption bands cannot be readily used to derive absolute mineral proportions, as complex effects of texture, grain size, and porosity also affect the spectra. Here, while the hydration band at 1.9 μm was observed at a strength up to ∼20% relative to the continuum, the absorption bands in the 2.1–2.5 μm range are faint (max. ∼5%), pointing to possibly low proportions of phyllosilicates, sulfates, and/or carbonates in the fields of view of the instrument.

From the VISIR spectra only, it is challenging to infer whether the Fe/Mg-carbonates detected at Séítah are hydrated as they are likely observed as mixtures with phyllosilicates, which exhibit strong water bands. Fe-carbonates are nominally anhydrous, whereas Mg-carbonates are more complex, with several hydrated forms found in nature, such as hydromagnesite or nesquehonite (whose stability in the Martian environment remains uncertain; Calvin et al., 1994; Harner & Gilmore, 2015). However, other than carbonates, similar minerals were observed between the Máaz and Séítah rocks without significant variation of the water band depth, suggesting a nonsignificant hydration of carbonates. This is consistent with LIBS data, in which carbonate detections are not associated with intense H emission lines compared to other targets (Clavé et al., 2022).

In Máaz, the 2.2 μm absorption possibly attributed to gypsum, Al-phyllosilicates or hydrated silica was observed at low intensity, close to the noise level (at ∼1.5% relative to the continuum), suggesting a minor influence of the corresponding hydrated mineral phase. Faint 2.32 μm absorptions are also observed and attributed to an Mg-OH phase, that could be an Mg-phyllosilicate and/or an Mg-hydroxide. In Máaz, the 2.32 μm absorption is faint and also close to the noise level (Figure 3), suggesting a weak contribution of potential Mg-phyllosilicates to the hydration. In Séítah, this band was observed at stronger intensity and was attributed to either carbonates, Mg-hydroxide, serpentine, Mg-smectite and/or talc. Talc, serpentine, and Mg-hydroxide spectra do not exhibit an absorption at 1.9 μm (or subdued in the case of serpentine) due to their lack of structural water and are not expected to bear on the structural hydration in Séítah.

Mg-sulfates are one candidate to explain the drop in reflectance past 2.3 μm observed here as well as the absorption at ∼2.13 μm. As the intensity of the 2.3 μm drop can be affected by thermal effects residuals after the calibration (Royer et al., 2022), we measured the depth of the 2.13 μm band (shouldered at 1.93 and 2.18 μm), as a means to track the signature of Mg-sulfate in the Máaz formation (Table 1). Figure 7b shows that this absorption is rarely observed and is associated with relatively low 1.9 μm band depths, with the exception of the abraded patch *Bellegarde*, suggesting a relatively low influence of Mg-sulfates in the VISIR spectra of rocks.

No correlation between the band center and the depth of the 1.9 μm absorption was observed (Figure 7b). However, the endmember spectrum of location #4 on *Bidziil* displays one of the strongest 1.9 μm band depths and is interpreted as consistent with Fe-phyllosilicate. Because the 1.9 μm absorption in nontronite and hisingerite spectra

is centered at lower wavelength (~1.91–1.92 μm) compared to the other hydrated mineral phases detected here (>1.93 μm), an Fe-phyllosilicate cannot alone explain the widespread hydration on the crater floor. The rocks of the Máaz formation have NIR spectral shapes consistent with hydrated Fe-bearing minerals (Figures 6 and 10), and it is likely that the main bearer of hydration consists of a mixture of Fe-phyllosilicate and Fe-oxyhydroxides (as also evidenced by ICA results). As shown above, the spectral signature of other candidate hydrated minerals (including sulfates and possibly Al-phyllosilicates, hydrated silica, perchlorate, and zeolites) appear less dominant on the spectral data set of Jezero's crater floor and hence probably have a minor influence on the hydration band observed at 1.9 μm.

5.2.1.1. Hydration of Rock Tailings and Soils

The wide diversity of targets measured by SuperCam revealed some variability in water band depth among different target types. In particular, the spectra of the tailings resulting from drill or abrasion activities often exhibit a subdued 1.9 μm water band compared to the spectra acquired on their corresponding natural rock surface (e.g., on the *Rochette* outcrop in Figure 12). Heating during drilling and abrasion is not sufficient to dehydrate the detected minerals. Hence, this could be due to a reduced proportion of hydrated phases with depth from an outer, more weathered surface to a more pristine interior. The reflectance spectra measured on rocks usually have weaker bands compared to their crushed equivalent, as particles are welded together (Hapke, 1993). Here, the tailings are very fine powders (aggregates of a few microns) favoring reduced optical paths, hence possibly reducing spectral contrast and absorption strengths. Overall, one can explain the different spectral shape of the rock tailings by a change of optical regime, and not necessarily by a less altered interior. We note that the spectra of *Rochette* and *Brac*'s tailings have a lower reflectance and spectral contrast compared to those of *Sid* and *Issole*. Because the spectra are not corrected for photometric effects, it is possible that the higher phase angles associated with the *Sid* and *Issole* observations (41–89°) compared to the *Rochette* and *Brac* observations (26–48°) might also be responsible for the difference (in that case, *Sid* and *Issole*'s tailings would be more backscattering than *Rochette* and *Brac*'s tailings).

We noted that the reflectance spectra measured by SuperCam on the soils of Jezero crater usually have weaker water absorption bands compared to the spectra of the crater floor rocks (Figure 7a). This is consistent with the low hydration levels inferred from NIR orbital spectra and the extensive soil coverage on the Cf-fr. However, in LIBS data, soil targets are associated with stronger H emission lines (Cousin, Meslin, et al., 2022), in apparent discrepancy with our results. The H signal in LIBS spectra is highly affected by matrix effects (e.g., Schröder et al., 2015), which could (at least partially) induce artificially stronger H signal in soils compared to rocks. Because the water absorption strength in the reflectance spectra is also influenced by factors not related to hydration (typically, the grain size or roughness of the sample) and considering the matrix effects affecting hydrogen in LIBS data, it is challenging to determine precisely how the hydration of the regolith compare to the Jezero crater floor rocks.

5.2.2. Alteration History

One of the implications of our study regarding the history of Jezero is that water-rock interactions affected the crater floor broadly, with hydrated minerals present to some degree in most of the rocks analyzed. The interpreted mineralogical assemblages represent a diversity of possible secondary mineral phases, with both Fe^{3+} and Mg-phyllosilicates, Fe-oxyhydroxides, carbonates, and sulfates. Al-phyllosilicates do not appear to be abundant (in agreement with orbital observations). These types of minerals appear to be common to the Máaz and Séítah units, implying a similar, possibly contemporaneous, alteration. The exception is the presence of carbonates, which seems to be restricted to the Séítah formation. Clavé et al. (2022) reported LIBS compositions consistent with their presence in Máaz rocks as well, but the corresponding carbonates occurrences appear to be scarce and at a lower proportion than in Séítah rocks—which from the intensity of the 2.5 μm absorption is probably very low.

In Séítah, a significant amount of the olivine of the protolith has been preserved, showing that aqueous alteration was likely limited in time, water/rock ratio, and/or intensity (controlled by e.g., temperature, pH), as olivine alters rapidly at geological timescales when interacting with liquid water (Stopar et al., 2006). In Máaz, no olivine has been detected in the LIBS data set, but we cannot exclude that it was fully dissolved and left voids in rocks (possibly allowing pore-space for deposition of sulfates). In both units, the presence of poorly crystalline mineral phases such as ferrihydrite points toward short-lived, low temperature water-rock interactions and/or limited diagenesis (Dehouck et al., 2017). This is in agreement with Wiens et al. (2022) analysis of LIBS data suggesting

limited leaching of water-soluble cations in the rocks of the crater floor. In the following section, we discuss early- and late-stage (pre-deposition and post-deposition of sulfates in pore space, respectively) alteration history.

5.2.2.1. Early-Stage Alteration

The occurrence of clay-minerals in both Máaz and Séítah rocks is consistent with the weathering of an Fe/Mg-bearing protolith, likely unrelated to the sulfate deposition environment. Here, the Fe^{3+}-clay mineral signature might be related to nontronite and/or hisingerite, which are spectrally similar. In this section, we discuss two hypotheses that could be compatible with the presence of these clay minerals and associated secondary minerals: supergene weathering or serpentinization.

Ferric clay minerals such as nontronite usually form under neutral to alkaline and oxidizing conditions, directly from weathering of the inital protolith (Gainey et al., 2017) or by precipitation of ferrous clay minerals under anoxic/reducing conditions and their subsequent oxidation (Chemtob et al., 2017; Harder, 1976). Here, the coupled detection of oxyhydroxides, likely in the ferrihydrite form, and the absence of Fe^{2+}-clays point toward oxidizing conditions in the alteration history, but the associated timing is uncertain. Fe^{3+}-clays could have been produced during oxidizing and low-temperature weathering of the protolith near the surface (possibly related to the lake activity); another possibility is that Fe^{2+} phyllosilicates first precipitated under anoxic conditions and were fully oxidized later in the history of the site.

On the other hand, the presence of hisingerite can imply different alteration environments. Though this mineral is relatively rare on Earth, it can be formed by supergene weathering but also during hydrothermal alteration of ferroan olivine-bearing rocks and has been proposed as a serpentinization product more common on Mars than on Earth owing to the higher Fe content of the Martian mantle (Evans et al., 2017; Tutolo et al., 2019). From orbit, Mg-serpentine has been detected in the regional olivine-bearing unit (Ehlmann et al., 2009). Brown et al. (2010) and Viviano-Beck et al. (2013) proposed that the widespread carbonates observed in this unit could result from serpentinization and carbonation processes acting on ultramafic rocks, from which talc and magnesite would have formed with serpentinized olivine. In this contribution, we show the detection of Fe/Mg-carbonates and an Mg–OH phase in Séítah rocks. The nature of the Mg–OH mineral is unclear and could possibly be, among other candidates, talc or serpentine. In laboratory, Mg-serpentine-bearing mineral mixtures show a distinctive absorption band at 2.32 μm but even in mixtures with low serpentine concentrations the band depth of this feature is greater than what has been observed by the SuperCam instrument thus far in the mission (Mandon et al., 2022). This suggests no evidence for elevated Mg-serpentine content in the rocks measured during the first year of the mission. Hence, in the serpentinization scenario, either most of the Mg-serpentine produced from olivine alteration has been converted to hisingerite (Tutolo et al., 2019) or talc and magnesite under CO_2-rich fluids and decreased temperature, or the rocks of Séítah never experienced conditions favorable to the production of Mg-serpentine from olivine. Nevertheless, the Séítah rocks appear relatively pristine (with a limited amount of weathering products), as evidenced by large amount of remaining olivine.

5.2.2.2. Late-Stage Alteration

Geochemical models performed by Chevrier and Morisson (2021) showed that the evaporation of fluids resulting from the weathering of an olivine and pyroxene protolith and subsequent precipitation of ferric clay minerals and oxyhydroxides does not produce significant concentrations of Ca-sulfates and is not associated with Mg-sulfates precipitation. The Mg-sulfates inferred from the infrared spectra of the Máaz and Séítah rocks may record an environment distinct from the weathering of the crater floor and production of all the other secondary mineral phases mentioned before. The deposition of high-solubility phases such as sulfates would likely correspond to the final aqueous activity at Jezero, during the late-stage evaporation of the lake, with sulfate deposition from concentrated brines into the pores of the rocks. Their possible presence on both the abraded rocks of Máaz and Séítah supports that most of the crater floor observed today was exposed to the surface waters (likely briefly, in order to support the low alteration of the olivine grains), or at least not deeply buried to allow percolation of fluids into the bedrock. The presence of akaganeite in Jezero is also consistent with past evaporitic conditions, likely in a highly saline and chlorinated environment.

In Jezero, near-infrared spectral similarities were observed between dusty targets and the purple-tinted material coating portions of some rocks of the crater floor. This suggests some shared compositional traits and potentially a genetic link between dust and the coatings. This could result from induration of dust particles on the surface of rocks by a fluid of unknown composition, later in the history of the crater floor. LIBS measurements on

these coatings show enrichment in S and H, in agreement with a hydrated sulfate component similar to the dust (Meslin et al., 2022). These coatings were observed sporadically on rocks from both formations of the crater floor (Garczynski et al., 2022), suggesting that at least minor liquid water was present after the formation of the Máaz rocks. This environment could have been repeated over extended periods of time to allow cementation of grains into coatings and balanced against erosion upon surface exposure. The fact that they are observed today on the surface of rocks affected by erosion implies that the last processes of coatings formation happened late in the history of Jezero. This late-stage interaction of water with the rock surfaces might explain the fact that salts were predominantly detected on abraded patches by both the VISIR and LIBS technique compared to the non-abraded rock surfaces, as salt dissolution is likely to occur with limited surface water (although other processes such as irradiation can slightly alter sulfates on the surface; e.g., Cloutis et al., 2007).

5.3. Origin of Regolith Materials

Cousin et al. (2015) showed that the soils analyzed at Gale crater along the MSL rover traverse are composed of various material families, with the coarsest fraction being likely sourced from physical weathering of the surrounding rocks and the finest fraction being composed of different materials. These fine soils have a basaltic composition, thought to be global on the surface of Mars (Yen et al., 2005). Notably, the same trend seems to be present for the soils of Jezero crater:

- the VISIR signature of the fine soils is consistent with the presence of pyroxene, with a weaker olivine component, similarly to the Martian global soils. The spectra measured on the fine soils at Jezero exhibit some weak absorptions near 2.3 μm and alternatively similar to those observed in rocks of the crater floor, suggesting some level of contamination of particles sourced from these rocks into the regolith;
- the coarsest soils are associated with a strong olivine signature, similarly to the Séítah rocks and implying that, as for the coarse soils of Gale crater, physical weathering of the surrounding rocks source the local regolith.

5.4. Comparison and Implications for NIR Orbital Studies

The evaluation of the reflectance between ∼1 and 2.5 μm is predominantly used from orbit to detect and map minerals on the surface of Mars and hence significantly supports the interpretation of past environments conditions (e.g., Bishop et al., 2008; Carter et al., 2013). The IRS onboard SuperCam was the first near-infrared reflectance spectrometer to operate directly on the surface of Mars, joined 3 months later by the MarSCoDe instrument on the Zhurong rover as part of the Tianwen-1 mission (Liu, Wu, et al., 2022). Therefore, it provides a prime opportunity to bring context to orbital studies using near-infrared data. Indeed, the spectra measured from orbit result from the combination of complex spectral mixing effects and of variable surface state at large scales, as the best spatial resolution of orbital hyperspectral cameras is on the order of ∼12 m/pixel (Kreisch et al., 2017). It should be noted that the comparison between in situ and orbital measurements (the latter being usually shown as ratios in the literature) is not straightforward and future work with SuperCam data will expand on this aspect. Here, we provide an initial report on the insights provided by the ground-based spectral signatures at Jezero crater, in order to understand the orbital ones.

5.4.1. Orbital Data Sets: Bedrock Exposures Versus Soils Signatures

The in situ analysis of the crater floor by the rover payload and in particular by the VISIR spectrometer of SuperCam has confirmed the presence of all the minerals detected from orbit in the region (i.e., olivine, carbonates and Fe/Mg-phyllosilicates). These minerals are present in the bedrock (as opposed to the regolith), validating the strength and ability of the NIR orbital data to provide useful information to assess rock lithologies and hence deduce geological history.

Perseverance's instruments analyses have revealed the presence of additional minerals that are theoretically detectable in the NIR. In particular, the rover payload has discovered the presence of sulfates (from LIBS, PIXL, and SHERLOC instruments data and in VISIR as shown here) and perchlorates on the crater floor (Meslin et al., 2022; Razzell Hollis et al., 2022). These minerals were not detected from orbit in Jezero or on its watershed, despite their signature being observed elsewhere on Mars (e.g., Gendrin et al., 2005; Massé et al., 2010). As polyhydrated sulfates lack unique absorption bands in the NIR range, difficulty may arise in their identification

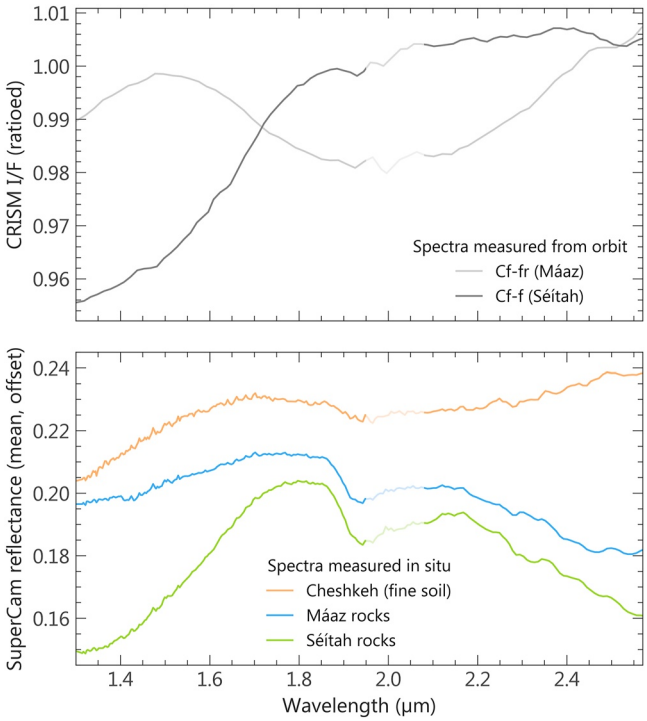

Figure 13. First-order comparison between in situ and orbital spectra of the crater floor. Orbital spectra were extracted from the Compact Reconnaissance Imaging Spectrometer for Mars instrument data by Goudge et al. (2015). Segments of the spectra shown with lower opacity line near 2 μm correspond to the main atmospheric CO_2 absorption domain, where residuals might affect the spectra.

and distinction from other hydrated minerals. Also, the signature of sulfates is relatively minor in our data set, hence possibly having a weak contribution to the spectra acquired from orbit as well.

A first-order comparison between the in situ reflectance signal of the crater floor units and spectra measured from orbit is provided in Figure 13. From orbital data, it was first hypothesized that the Máaz formation (or the Cf-fr) was igneous in nature, based on its crater-retaining morphology and its near-infrared spectral signature consistent with a mixture of pyroxene and olivine (Goudge et al., 2015). Later, it was noted that a sedimentary origin could not be discarded based on the morphology solely (Stack et al., 2020); however, it was not understood whether the spectral signature of mafic minerals originates from the bedrock or from surficial deposits, despite the unit having a smooth texture on high-resolution orbital images that one could interpret as extensive soil coverage (Horgan et al., 2020). Investigation by the Mars 2020 payload has now confirmed the basaltic composition of the Máaz formation. However, no olivine has been observed, and we have shown here that the spectral signature of the bedrock in the near-infrared is dominated by hydrated minerals, with so far no single-point spectrum consistent with a mixture of olivine and pyroxene. On the other hand, NIR single-point spectra of soils exhibit the same features as the spectra measured by Goudge et al. (2015), with both olivine and pyroxene identified. This suggests that the mafic nature of the Máaz formation that was inferred from orbit could in fact be due to the major contribution of soils within CRISM pixels, which dominate the spectral signal in this extensively mantled area. In other words, the Mars 2020 mission confirmed the igneous composition of the Máaz formation that was inferred from orbit but also revealed that the signature of mafic minerals detected with CRISM was more likely the signature of the regolith that extensively covers the Máaz bedrock. This highlights some implications for the interpretation of similar spectral signatures elsewhere on Mars, as fine soils tends to have an overall composition common to different locations on the planet (Cousin et al., 2015).

Wright et al. (2022) demonstrated that the surficial covers of Máaz and Séítah are significantly different, with the Máaz surface being mostly composed of scarce bedrock exposures and soils and the Séítah surface of scarce bedrock exposures and large sand ripples. We showed that the sand dunes that are widely covering the Séítah formation seem to be composed of material sourced from the local bedrock. This might explain why the bedrock signature is dominating the orbital spectra measured over Séítah, as opposed to Máaz.

Using CRISM data, Horgan et al. (2020) noted an apparent enrichment of olivine along the rover traverse, compared to the rest of the Cf-fr. We showed that no rock of the Máaz formation exhibit an olivine signature in the VISIR, while parts of its regolith consists of fine grains with mm-sized granules associated with a signature of olivine and secondary minerals, similarly to Séítah rocks. Hence, a scenario where the erosion of the nearby Séítah bedrock would provide material input onto the Cf-fr as eolian bedforms is highly plausible, compared to an actual olivine enrichment of the Máaz bedrock near the contact with Séítah (Cousin, Meslin, et al., 2022; Vaughan et al., 2021).

Finally, the rocks of the crater floor exhibit a stronger hydration band at ∼1.9 μm compared to orbital measurements. This is consistent with the signature of rocks being diluted in the pixels of the orbital imaging spectrometers, which at best resolution integrate tens of square meters of surface, where bedrock exposures are relatively scarce. A similar effect was noted in the analysis of the NIR spectra measured by the Zhurong rover (Liu, Wu, et al., 2022), in an area which does not exhibit hydrated features from orbit.

5.4.2. Impact of the Martian Dust

On Mars, one of the main limiting factors to identify minerals from hyperspectral orbital data is the presence of aerial and surface dust, which impedes the spectral signatures of the rocks on the surface. While the signature

of dust in VISIR reflectance has been estimated on dusty terrains (e.g., Le Mouélic et al., 2006), data from the SuperCam instrument offer the first opportunity to measure its near-infrared spectral signature in situ. Surprisingly, even the dustiest targets exhibit a 1.9 μm absorption related to water (caused by some hydrated mineral or water adsorbed on the surface of the small dust particles), that does not seem to be related to the rocks underneath. This contrasts with previous assumptions, based on orbital studies, that the dust is spectrally neutral in the NIR below 2.5 μm, although the 3 μm fundamental absorption of water observed globally on the surface did suggest some form of hydration (Audouard et al., 2014). Similar to orbital measurements, a subtle downturn past 2.3 μm was observed, possibly related to the presence of some water-bearing materials. The effects of the atmosphere and aerosols (decreasing spectral contrast) could explain these discrepancies between the orbital and in situ data. Also, we note that the in situ observations might be impacted by multiple scattering leading to a 1.9 μm signature for dust.

Notably, the magnetic dust deposited on the edges of the calibration targets does exhibit a strong red slope in the visible but a flat and featureless spectrum in the near-infrared and no H_2O and OH related absorptions (Section 4.1). One possibility is that the magnetic dust (i.e., the fraction of dust attracted by the magnets, enclosing the SCCT) does not include hydrated phases (but mainly maghemite/magnetite). Another explanation is that the dust coatings present on the surrounding rocks are sufficiently older to allow for hydration, perhaps as part of induration processes.

5.5. First Near-Infrared Spectrometer on the Surface: Lessons Learned After 1 Year of Measurement

During the first year of the mission, the reflectance point spectrometer of SuperCam demonstrated considerable utility in inferring in a nondestructive way the presence of a variety of primary and secondary minerals. Compensation for instrumental effects, variable illumination and observation conditions, and atmospheric corrections enabled constraints on surface mineralogy (albeit not always unique), even when mixtures within the instrument fields of view complicated mineral identification.

Mineralogical detections with VISIR are consistent with LIBS data (e.g., olivine, pyroxene, Fe-oxides, Fe/Mg-carbonates, and Mg-sulfates; Clavé et al., 2022; Meslin et al., 2022; Wiens et al., 2022), albeit with some differences. In particular, the detections of minerals with one technique or the other are not necessarily associated with the same point in a raster, but often occur for the same target or rock type, likely owing to a significant difference of analytical footprint between VISIR and LIBS. ICA was proven quite relevant to separate individual spectral signatures from mineralogical endmembers when applied to IRS data. It allowed the identification of additional minerals, while the reflectance signal was dominated by the signature of hydrated phases: in particular, pyroxenes, which appear to be abundant based on the data of the SuperCam's LIBS and the PIXL instrument (Razzell Hollis et al., 2022; Wiens et al., 2022), were not readily identified in the VISIR point spectra. Using the reflectance spectra, we were able to detect minerals not identified with LIBS data, such as the ferric phyllosilicates present in most of the rocks of the crater floor and which have implications for understanding the past aqueous environment at Jezero crater.

Ratios of SuperCam spectra were shown to be effective at emphasizing particular mineral phases present in the rocks, as was comparison of point spectra with mineral spectral libraries and band matching. However, ratioing was successful for mineralogical interpretation for only a limited set of observations, compared to orbital studies where it is conventionally performed (e.g., Horgan et al., 2020). To assist the retrieval of the different signatures of the minerals mixed in a rock spectrum, additional efforts are needed to document natural rock and mineral mixture spectra (e.g., Bishop et al., 2013; Lantz et al., 2020; Mandon et al., 2022), as well as to understand the physics behind natural rock spectroscopy (e.g., Carli & Sgavetti, 2011; Carli et al., 2015; Harloff & Arnold, 2001). These will likely provide valuable insights to understand future data acquired by SuperCam or by other point spectrometers onboard planetary exploration missions (e.g., Korablev et al., 2017; Liu, Wu, et al., 2022; Xu et al., 2021). Ultimately, spectral unmixing (linear and unlinear) shall provide better constraints on the modal mineralogy and on the formation processes of the rocks and soils (Poulet et al., 2022).

6. Conclusion

In this work, we reported the first-year results of the first reflectance spectrometer on the Martian surface covering the VISIR range from 1.3 to 2.6 μm, onboard the Perseverance rover of the Mars 2020 mission. In particular, we measured the reflectance spectra of rocks of the floor of Jezero crater, including the rocks that were cached for a possible return to Earth, as well as soils and dust coatings. From these results, we identified the following:

- the basaltic upper part of Jezero's floor stratigraphy, informally referred to as the Máaz formation, exhibits a spectral signature in the VISIR dominated by hydrous mineral phases: Fe-oxyhydroxides (e.g., ferrihydrite, akaganeite), Fe^{3+}-phyllosilicates (nontronite and/or hisingerite), monohydrated Mg-sulfates (e.g., kieserite), potential polyhydrated sulfates, and some minor Mg–OH phase(s) (e.g., Mg-smectite, serpentine, talc, and/or brucite). Primary minerals were also detected by the spectrometer and consist of high-Ca pyroxenes (felspars being mostly featureless in the VISIR). No olivine was observed, in agreement with LIBS observations (Udry et al., 2022; Wiens et al., 2022);
- this mineralogical assemblage transitions into more mafic minerals toward the lowest stratigraphic levels observed, in the cumulate olivine-bearing formation called Séítah. Strong olivine signatures were observed in the reflectance data, along with high-Ca pyroxene and a complex mixture of alteration/hydrated mineral phases consisting of Fe-oxyhydroxides, Fe^{3+}-phyllosilicates (nontronite and/or hisingerite), some Mg–OH phase(s) (e.g., Mg-smectite, serpentine, brucite, and/or talc), scarce Fe/Mg-carbonates, an Al or Si–OH-phase, as well as monohydrated Mg-sulfates;
- alteration/hydrated minerals are present at relatively low proportion in the rocks (a few wt.% maximum) but their presence was evident in most of the rocks analyzed, pointing toward a widespread aqueous alteration of the crater floor but limited in intensity and/or time, as also evidenced by the dominance of poorly crystalline mineral phases such as ferrihydrite and the lack of Al-phyllosilicates. The proposed alteration sequence of the Máaz formation includes weathering of the basaltic protolith from surface/near-surface leaching of the rocks, possibly related to the lake activity or under deeper hydrothermal serpentinizing conditions, and under neutral to alkaline conditions. The presence of clay minerals usually favors the concentration and preservation of organic matter, though oxidizing conditions (as evidenced by the presence of Fe^{3+}-phyllosilicates and oxides) might have acted as a degradation process of organic materials. The strong olivine spectral features and weak secondary minerals signatures suggest that, as for the Máaz formation, water-rock interactions were likely minor in Séítah. Finally, evaporation of the lake likely induced minor sulfate deposition from concentrated brines onto pores of the rocks of the crater floor;
- most of the minerals detected from orbit (olivine, pyroxene, Fe/Mg-phyllosilicates, Fe/Mg-carbonates, and akaganeite; Carter et al., 2022; Goudge et al., 2015; Horgan et al., 2020) are present in the bedrock (as opposed to the regolith), validating the strength and ability of the NIR orbital data to provide useful information to assess rock lithologies and hence deduce geological history;
- fine soils of the crater floor exhibit spectra suggesting a major mineralogical composition consistent with what was inferred elsewhere on Mars, with pyroxene and possibly olivine, as well as a hydrous component, possibly inherited from the surrounding rocks. The regolith signature is likely what dominates orbital observations of the Máaz formation, whose origin was thought to be igneous on the basis of morphological and spectral criteria (Goudge et al., 2015). Similarities between spectra measured on rocks and on coarse-grained soils suggest significant local input from the Séítah formation onto the Máaz formation as eolian bedforms, and resolves the origin of the orbital signature of olivine-bearing materials on the western Máaz formation (Horgan et al., 2020);
- the first in situ near-infrared spectra of the Martian dust reveal similar features compared to dusty terrains measured from orbit, with a red slope in the visible range and overall flat spectra in the near-infrared range. However, a subtle hydration band at 1.9 μm is always present, which differs from orbital spectra and reveals a more significant contribution of hydration to the Martian surface dust signature than previously thought. The spectral similarity between dust and the purple-tinted coatings observed on the rocks of the crater floor suggests a similar composition between the two materials and potential widespread past processes of dust induration under surface liquid water activity late in the history of Jezero;
- of interest for the Mars Sample Return mission, all four pairs of rock sampled on the crater floor of Jezero during the first year of the Mars 2020 mission exhibit spectral features representative of the diversity of the spectra measured on the two geological units investigated by the rover.

Orbital data suggest that Perseverance landed in a relatively low hydration region and that the rover will be driving through areas of progressively increasing hydration throughout the mission, as it moves onto the delta, the marginal carbonate unit and the region outside of Jezero crater. Sample return and future in situ measurements on these potentially more hydrated and/or diverse rocks are expected to bring new insights into the past environment at Jezero crater.

Appendix A

R. C. Wiens[1,2], S. Maurice[3], T. Acosta-Maeda[4], C. Alvarez-Llamas[5], R. B. Anderson[6], S. M. Angel[7], D. M. Applin[8], G. Arana[9], M. Bassas-Portus[10], R. Beal[1], P. Beck[11], K. Benzerara[12], S. Bernard[12], P. Bernardi[13], T. Bertrand[13], O. Beyssac[12], T. Bosak[14], B. Bousquet[15], A. Brown[16], A. Cadu[10], P. Caïs[17], K. Castro[9], B. Chide[1], E. Clavé[15], S. M. Clegg[1], E. Cloutis[8], S. Connell[8], A. Cousin[3], A. Debus[18], E. Dehouck[19], D. Delapp[1], C. Donny[18], A. Dorresoundiram[13], G. Dromart[19], B. Dubois[20], C. Fabre[21], A. Fau[3], W. Fischer[22], O. Forni[3], T. Fouchet[13], R. Francis[23], J. Frydenvang[24], T. Gabriel[6], O. Gasnault[3], E. Gibbons[25], I. Gontijo[23], X. Jacob[26], J. R. Johnson[27], H. Kalucha[22], E. Kelly[4], E. W. Knutsen[28], G. Lacombe[28], N. L. Lanza[1], J. Laserna[5], J. Lasue[3], S. Le Mouélic[29], C. Legett IV[1], R. Leveille[25], E. Lewin[11], G. Lopez-Reyes[30], R. D. Lorenz[27], E. Lorigny[18], J. M. Madariaga[9], M. Madsen[24], S. Madsen[23], L. Mandon[13], N. Mangold[29], M. Mann[18], J.-A. Manrique[3,30], J. Martinez-Frias[31], L. E. Mayhew[32], T. McConnochie[33], S. M. McLennan[34], N. Melikechi[35], P.-Y. Meslin[3], F. Meunier[18], D. Mimoun[10], G. Montagnac[19], F. Montmessin[28], J. Moros[5], V. Mousset[18], N. Murdoch[10], T. Nelson[1], R. T. Newell[1], A. Ollila[1], Y. Parot[3], P. Pilleri[3], C. Pilorget[36,37], P. Pinet[3], G. Pont[18], F. Poulet[36], C. Quantin-Nataf[19], B. Quertier[17], W. Rapin[3], A. Reyes-Newell[1], S. Robinson[1], L. Rochas[18], C. Royer[13], F. Rull[30], V. Sautter[12], S. Schröder[38], S. Sharma[4], V. Shridar[23], A. Sournac[10], A. Stott[10], M. Toplis[3], I. Torre-Fdez[9], N. Turenne[8], T. Tzanetos[23], A. Udry[39], M. Veneranda[30], D. Venhaus[1], D. Vogt[38], and P. Willis[23]

[1]Space and Planetary Exploration Team, Los Alamos National Laboratory, Los Alamos, NM, USA. [2]Earth, Atmospheric, and Planetary Sciences, Purdue University, West Lafayette, IN, USA. [3]Institut de Recherche en Astrophysique et Planétologie, Université de Toulouse 3 Paul Sabatier, CNRS, CNES, Toulouse, France. [4]University of Hawai'i at Mānoa, Manoa, HI, USA. [5]Universidad de Malaga, Malaga, Spain. [6]U.S. Geological Survey, Flagstaff, AZ, USA. [7]Department of Chemistry and Biochemistry, University of South Carolina, Columbia, SC, USA. [8]University of Winnipeg, Winnipeg, MB, Canada. [9]University of Basque Country, UPV/EHU, Leioa, Bilbao, Spain. [10]Institut Supérieur de l'Aéronautique et de l'Espace (ISAE-SUPAERO), Université de Toulouse, Toulouse, France. [11]Institut de Planétologie et Astrophysique de Grenoble, CNRS, Univ. Grenoble Alpes, Grenoble, France. [12]Institut de Minéralogie, de Physique des Matériaux et de Cosmochimie, CNRS, Sorbonne Université, MNHN, Paris, France. [13]Laboratoire d'Etudes Spatiales et d'Instrumentation en Astrophysique, Obs. Paris, CNRS, Sorbonne Univ., Univ. Paris-Diderot, Meudon, France. [14]Earth, Atmospheric and Planetary Sciences, Massachusetts Institute of Technology, Cambridge, MA, USA. [15]Center Lasers Intenses et Applications, CNRS, CEA, Univ. Bordeaux, Bordeaux, France. [16]Plancius Research, Severna Park, MD, USA. [17]Laboratoire d'Astrophysique de Bordeaux, CNRS, Univ. Bordeaux, Bordeaux, France. [18]Center National d'Etudes Spatiales, Toulouse, France. [19]Univ. Lyon, UCBL, ENSL, UJM, CNRS, LGL-TPE, Villeurbanne, France. [20]Groupe d'Instrumentation Scientifique, Observatoire Midi-Pyrénées, Toulouse, France. [21]GéoRessources, CNRS, Univ. Lorraine, Nancy, France. [22]California Institute of Technology, Pasadena, CA, USA. [23]Jet Propulsion Laboratory, California Institute of Technology, Pasadena, CA, USA. [24]University of Copenhagen, Copenhagen, Denmark. [25]McGill University, Montreal, QC, Canada. [26]Institut de Mécanique des Fluides, Univ. Toulouse 3 Paul Sabatier, INP, CNRS, Toulouse, France. [27]Space Exploration Sector, Johns Hopkins Applied Physics Laboratory, Laurel, MD, USA. [28]Laboratoire Atmosphères, Milieux, Observations Spatiales, CNRS, Univ. Saint-Quentin-en-Yvelines, Sorbonne Univ., Guyancourt, France. [29]Laboratoire Planétologie et Géosciences, CNRS, Université Nantes, Université Angers, Nantes, France. [30]University of Valladolid, Valladolid, Spain. [31]Agencia Estatal Consejo Superior de Investigaciones Científicas, Madrid, Spain. [32]Department of Geological Sciences, University of Colorado Boulder, Boulder, CO, USA. [33] University of Maryland, College Park, MD, USA. [34]State University of New York, Stony Brook, NY, USA. [35]Department of Physics and Applied Physics, Kennedy College of Sciences, University of Massachusetts, Amherst, MA, USA. [36]Institut d'Astrophysique Spatiale, CNRS, Univ. Paris-Saclay, Orsay, France. [37]Institut Universitaire de France, Paris, France. [38]Deutsches Zentrum für Luft- und Raumfahrt (DLR), Institute of Optical Sensor Systems, Berlin, Germany. [39]University of Nevada Las Vegas, Las Vegas, NV, USA.

Conflict of Interest

The authors declare no conflicts of interest relevant to this study.

Data Availability Statement

All data are available in the NASA Planetary Data System (Beegle, 2021; Bell & Maki, 2020; Maki, 2021; Maurice & Wiens, 2021).

Acknowledgments
The authors are truly grateful for the SuperCam and Mars 2020 hardware operations teams for their investment in the mission. This work was supported by the CNES. Additional funding was provided by the following sources: NASA's Mars exploration program, CNES, CNRS, IRIS OCAV, DIM ACAV, CSA, NSERC, and ASI (ASI/INAF Grant 2017-48-H-0). The authors thank B. Bultel and another anonymous referee for improving the quality of the manuscript with their helpful feedbacks.

References

Audouard, J., Poulet, F., Vincendon, M., Milliken, R. E., Jouglet, D., Bibring, J.-P., et al. (2014). Water in the Martian regolith from OMEGA/Mars Express. *Journal of Geophysical Research: Planets*, *119*(8), 1969–1989. https://doi.org/10.1002/2014JE004649

Beegle, L. (2021). *Mars 2020 SHERLOC bundle*. NASA Planetary Data System. https://doi.org/10.17189/1522643

Bell, J. F., III, Glotch, T. D., Hamilton, V. E., McConnochie, T., McCord, T., McEwen, A., et al. (2008). Visible to near-IR multispectral orbital observations of Mars. In *The Martian surface-composition, mineralogy, and physical properties* (p. 169). Cambridge University Press.

Bell, J. F., III, & Maki, J. N. (2020). *Mars 2020 mast camera zoom bundle, from Arizona State University Mastcam-Z instrument team, calibrated products*. NASA Planetary Data System. https://doi.org/10.17189/Q3TS-C749

Bell, J. F., III, Maki, J. N., Mehall, G. L., Ravine, M. A., Caplinger, M. A., Bailey, Z. J., et al. (2021). The Mars 2020 *Perseverance* rover Mast Camera Zoom (Mastcam-Z) multispectral, stereoscopic imaging investigation. *Space Science Reviews*, *217*(1), 24. https://doi.org/10.1007/s11214-020-00755-x

Beyssac, O., Gasnault, O., Chide, B., Clave, E., Cousin, A., Forni, O., et al. (2021). Mafic chemistry and mineralogy (including olivine) of the coarse-grained regolith analyzed by SuperCam at Jezero crater, Mars. In *Presented at the AGU fall meeting* (pp. P25A–08).

Bhartia, R., Beegle, L. W., DeFlores, L., Abbey, W., Razzell Hollis, J., Uckert, K., et al. (2021). Perseverance's scanning habitable environments with Raman and luminescence for organics and chemicals (SHERLOC) investigation. *Space Science Reviews*, *217*(4), 58. https://doi.org/10.1007/s11214-021-00812-z

Bishop, J. L. (2020). Visible and near-infrared reflectance spectroscopy laboratory spectra of geologic materials. In J. L. Bishop, J. F. Bell III, & J. E. Moersch (Eds.), *Remote compositional analysis – Techniques for understanding spectroscopy, mineralogy, and geochemistry of planetary surfaces*. Cambridge University Press.

Bishop, J. L., Dobrea, E. Z. N., McKeown, N. K., Parente, M., Ehlmann, B. L., Michalski, J. R., et al. (2008). Phyllosilicate diversity and past aqueous activity revealed at Mawrth Vallis, Mars. *Science*, *321*(5890), 830–833. https://doi.org/10.1126/science.1159699

Bishop, J. L., Perry, K. A., Dyar, M. D., Bristow, T. F., Blake, D. F., Brown, A. J., & Peel, S. E. (2013). Coordinated spectral and XRD analyses of magnesite-nontronite-forsterite mixtures and implications for carbonates on Mars. *Journal of Geophysical Research: Planets*, *118*(4), 635–650. https://doi.org/10.1002/jgre.20066

Bishop, J. L., Quinn, R., & Dyar, M. D. (2014). Spectral and thermal properties of perchlorate salts and implications for Mars. *American Mineralogist*, *99*(8–9), 1580–1592. https://doi.org/10.2138/am.2014.4707

Bramble, M. S., Mustard, J. F., & Salvatore, M. R. (2017). The geological history of northeast Syrtis Major, Mars. *Icarus*, *293*, 66–93. https://doi.org/10.1016/j.icarus.2017.03.030

Brown, A. J., Hook, S. J., Baldridge, A. M., Crowley, J. K., Bridges, N. T., Thomson, B. J., et al. (2010). Hydrothermal formation of clay-carbonate alteration assemblages in the Nili Fossae region of Mars. *Earth and Planetary Science Letters*, *297*(1), 174–182. https://doi.org/10.1016/j.epsl.2010.06.018

Brown, A. J., Kah, L., Mandon, L., Wiens, R., Pinet, P., Clavé, E., et al. (2022). Properties of the Nili Fossae Olivine-clay-carbonate lithology: Orbital and in situ at Seitah. *arXiv*. https://doi.org/10.48550/arXiv.2206.13380

Brown, A. J., Viviano, C. E., & Goudge, T. A. (2020). Olivine-carbonate mineralogy of the Jezero crater region. *Journal of Geophysical Research: Planets*, *125*(3), e2019JE006011. https://doi.org/10.1029/2019JE006011

Burns, R. G. (1993). *Mineralogical applications of crystal field theory*. Cambridge University Press.

Calvin, W. M., King, T. V. V., & Clark, R. N. (1994). Hydrous carbonates on Mars?: Evidence from Mariner 6/7 infrared spectrometer and ground-based telescopic spectra. *Journal of Geophysical Research*, *99*(E7), 14659–14675. https://doi.org/10.1029/94JE01090

Cardoso, J. F., & Souloumiac, A. (1993). Blind beamforming for non-Gaussian signals. *IEE Proceedings F (Radar and Signal Processing)*, *140*(6), 362–370. https://doi.org/10.1049/ip-f-2.1993.0054

Carli, C., Serventi, G., & Sgavetti, M. (2015). VNIR spectral characteristics of terrestrial igneous effusive rocks: Mineralogical composition and the influence of texture. *Geological Society, London, Special Publications*, *401*(1), 139–158. https://doi.org/10.1144/SP401.19

Carli, C., & Sgavetti, M. (2011). Spectral characteristics of rocks: Effects of composition and texture and implications for the interpretation of planet surface compositions. *Icarus*, *211*(2), 1034–1048. https://doi.org/10.1016/j.icarus.2010.11.008

Carter, J., Loizeau, D., Mangold, N., Poulet, F., & Bibring, J.-P. (2015). Widespread surface weathering on early Mars: A case for a warmer and wetter climate. *Icarus*, *248*, 373–382. https://doi.org/10.1016/j.icarus.2014.11.011

Carter, J., & Poulet, F. (2013). Ancient plutonic processes on Mars inferred from the detection of possible anorthositic terrains. *Nature Geoscience*, *6*(12), 1008–1012. https://doi.org/10.1038/ngeo1995

Carter, J., Poulet, F., Bibring, J.-P., Mangold, N., & Murchie, S. (2013). Hydrous minerals on Mars as seen by the CRISM and OMEGA imaging spectrometers: Updated global view. *Journal of Geophysical Research: Planets*, *118*(4), 831–858. https://doi.org/10.1029/2012JE004145

Carter, J., Riu, L., Poulet, F., Bibring, J.-P., Langevin, Y., & Gondet, B. (2022). A Mars orbital catalog of aqueous alteration signatures (MOCAAS). *Icarus*, *389*, 115164. https://doi.org/10.1016/j.icarus.2022.115164

Carter, J., Viviano-Beck, C., Loizeau, D., Bishop, J., & Le Deit, L. (2015). Orbital detection and implications of akaganéite on Mars. *Icarus*, *253*, 296–310. https://doi.org/10.1016/j.icarus.2015.01.020

Chemtob, S. M., Nickerson, R. D., Morris, R. V., Agresti, D. G., & Catalano, J. G. (2017). Oxidative alteration of ferrous smectites and implications for the redox evolution of early Mars. *Journal of Geophysical Research: Planets*, *122*(12), 2469–2488. https://doi.org/10.1002/2017JE005331

Chevrier, V. F., & Morisson, M. (2021). Carbonate-phyllosilicate parageneses and environments of aqueous alteration in Nili Fossae and Mars. *Journal of Geophysical Research: Planets*, *126*(4), e2020JE006698. https://doi.org/10.1029/2020JE006698

Clark, R. N., & Roush, T. L. (1984). Reflectance spectroscopy: Quantitative analysis techniques for remote sensing applications. *Journal of Geophysical Research*, *89*(B7), 6329–6340. https://doi.org/10.1029/JB089iB07p06329

Clavé, E., Benzerara, K., Meslin, P.-Y., Forni, O., Royer, C., Mandon, L., et al. (2022). Carbonate detection with SuperCam in igneous rocks on the floor of Jezero crater, Mars. *Journal of Geophysical Research: Planets*, *127*, e2022JE007463. https://doi.org/10.1029/2022je007463

Clénet, H., Pinet, P., Daydou, Y., Heuripeau, F., Rosemberg, C., Baratoux, D., & Chevrel, S. (2011). A new systematic approach using the Modified Gaussian Model: Insight for the characterization of chemical composition of olivines, pyroxenes and olivine–pyroxene mixtures. *Icarus*, *213*(1), 404–422. https://doi.org/10.1016/j.icarus.2011.03.002

Cloutis, E. A., Craig, M. A., Mustard, J. F., Kruzelecky, R. V., Jamroz, W. R., Scott, A., et al. (2007). Stability of hydrated minerals on Mars. *Geophysical Research Letters*, *34*(20), L20202. https://doi.org/10.1029/2007GL031267

Cloutis, E. A., & Gaffey, M. J. (1991). Spectral-compositional variations in the constituent minerals of mafic and ultramafic assemblages and remote sensing implications. *Earth, Moon, and Planets*, *53*(1), 11–53. https://doi.org/10.1007/BF00116217

Cousin, A., Meslin, P. Y., Hausrath, E. M., Cardarelli, E., Lasue, J., Forni, O., et al. (2022). Soil diversity at Mars: Comparison of dataset from Gale and Jezero craters. In *Presented at the 53rd lunar and planetary conference (LPI contribution no. 1374)*.

Cousin, A., Meslin, P. Y., Wiens, R. C., Rapin, W., Mangold, N., Fabre, C., et al. (2015). Compositions of coarse and fine particles in Martian soils at gale: A window into the production of soils. *Icarus*, *249*, 22–42. https://doi.org/10.1016/j.icarus.2014.04.052

Cousin, A., Sautter, V., Fabre, C., Dromart, G., Montagnac, G., Drouet, C., et al. (2022). SuperCam calibration targets on board the Perseverance rover: Fabrication and quantitative characterization. *Spectrochimica Acta Part B: Atomic Spectroscopy*, *188*, 106341. https://doi.org/10.1016/j.sab.2021.106341

Crowley, J. K. (1986). Visible and near-infrared spectra of carbonate rocks: Reflectance variations related to petrographic texture and impurities. *Journal of Geophysical Research*, *91*(B5), 5001–5012. https://doi.org/10.1029/JB091iB05p05001

Dehouck, E., McLennan, S. M., Sklute, E. C., & Dyar, M. D. (2017). Stability and fate of ferrihydrite during episodes of water/rock interactions on early Mars: An experimental approach. *Journal of Geophysical Research: Planets*, *122*(2), 358–382. https://doi.org/10.1002/2016JE005222

Edgett, K. S. (2018). A two-decade journey, learning to recognize that Mars has a vast and accessible sedimentary rock record. In *Presented at the GSA annual meeting*.

Ehlmann, B. L., Mustard, J. F., Murchie, S. L., Poulet, F., Bishop, J. L., Brown, A. J., et al. (2008). Orbital identification of carbonate-bearing rocks on Mars. *Science*, *322*(5909), 1828–1832. https://doi.org/10.1126/science.1164759

Ehlmann, B. L., Mustard, J. F., Swayze, G. A., Clark, R. N., Bishop, J. L., Poulet, F., et al. (2009). Identification of hydrated silicate minerals on Mars using MRO-CRISM: Geologic context near Nili Fossae and implications for aqueous alteration. *Journal of Geophysical Research*, *114*(E2), E00D08. https://doi.org/10.1029/2009JE003339

Evans, B. W., Kuehner, S. M., Joswiak, D. J., & Cressey, G. (2017). Serpentine, Iron-rich phyllosilicates and fayalite produced by hydration and Mg depletion of peridotite, Duluth Complex, Minnesota, USA. *Journal of Petrology*, *58*(3), 495–512. https://doi.org/10.1093/petrology/egx024

Farley, K. A., Stack, K. M., Shuster, D. L., Horgan, B. H. N., Hurowitz, J. A., Tarnas, J. D., et al. (2022). Aqueously altered igneous rocks sampled on the floor of Jezero crater, Mars. *Science*, *377*(6614), eabo2196. https://doi.org/10.1126/science.abo2196

Farley, K. A., Williford, K. H., Stack, K. M., Bhartia, R., Chen, A., de la Torre, M., et al. (2020). Mars 2020 mission overview. *Space Science Reviews*, *216*(8), 142. https://doi.org/10.1007/s11214-020-00762-y

Fassett, C. I., & Head, J. W. (2005). Fluvial sedimentary deposits on Mars: Ancient deltas in a crater lake in the Nili Fossae region. *Geophysical Research Letters*, *32*(14), L14201. https://doi.org/10.1029/2005GL023456

Fau, A., Beyssac, O., Gauthier, M., Meslin, P. Y., Cousin, A., Benzerara, K., et al. (2019). Pulsed laser-induced heating of mineral phases: Implications for laser-induced breakdown spectroscopy combined with Raman spectroscopy. *Spectrochimica Acta Part B: Atomic Spectroscopy*, *160*, 105687. https://doi.org/10.1016/j.sab.2019.105687

Fergason, R. L., Hare, T. M., Mayer, D. P., Galuszka, D. M., Redding, B. L., Smith, E. D., et al. (2020). Mars 2020 terrain relative navigation flight product generation: Digital terrain model and orthorectified image mosaic. In *Presented at the 51st annual lunar and planetary science conference (LPI contribution no. 2020)*.

Fouchet, T., Reess, J.-M., Montmessin, F., Hassen-Khodja, R., Nguyen-Tuong, N., Humeau, O., et al. (2022). The SuperCam infrared spectrometer for the Perseverance rover of the Mars2020 mission. *Icarus*, *373*, 114773. https://doi.org/10.1016/j.icarus.2021.114773

Gainey, S. R., Hausrath, E. M., Adcock, C. T., Tschauner, O., Hurowitz, J. A., Ehlmann, B. L., et al. (2017). Clay mineral formation under oxidized conditions and implications for paleoenvironments and organic preservation on Mars. *Nature Communications*, *8*(1), 1230. https://doi.org/10.1038/s41467-017-01235-7

Garczynski, B. J., Bell, J. F., III, Horgan, B. H. N., Johnson, J. R., Rice, M. S., Vaughan, A., et al. (2022). Perseverance and the purple coating: A mastcam-Z multispectral story. In *Presented at the 53rd lunar and planetary conference (LPI contribution no. 2346)*.

Gasnault, O., Virmontois, C., Maurice, S., Wiens, R., Le Mouélic, S., Bernardi, P., et al. (2021). What SuperCam will see: The remote micro-imager aboard perseverance. In *Presented at the 52nd lunar and planetary science conference (LPI contribution no. 2248)*.

Gendrin, A., Mangold, N., Bibring, J.-P., Langevin, Y., Gondet, B., Poulet, F., et al. (2005). Sulfates in Martian layered terrains: The OMEGA/Mars Express view. *Science*, *307*(5715), 1587–1591. https://doi.org/10.1126/science.1109087

Goudge, T. A., Mustard, J. F., Head, J. W., Fassett, C. I., & Wiseman, S. M. (2015). Assessing the mineralogy of the watershed and fan deposits of the Jezero crater paleolake system, Mars. *Journal of Geophysical Research: Planets*, *120*(4), 2014JE004782. https://doi.org/10.1002/2014JE004782

Hanley, J., Chevrier, V. F., Davis, B. L., Altheide, T. S., & Francis, A. (2009). Reflectance spectra of low-temperature chloride and perchlorate hydrates and their relevance to the Martian surface. In *Presented at the the new Martian chemistry workshop*.

Hapke, B. (1993). *Theory of reflectance and emittance spectroscopy*. Cambridge University Press. Retrieved from https://www.cambridge.org/core/books/theory-of-reflectance-and-emittance-spectroscopy/4DE2B656DD8CCD9F75F12C66128D83D2

Harder, H. (1976). Nontronite synthesis at low temperatures. *Chemical Geology*, *18*(3), 169–180. https://doi.org/10.1016/0009-2541(76)90001-2

Harloff, J., & Arnold, G. (2001). Near-infrared reflectance spectroscopy of bulk analog materials for planetary crust. *Planetary and Space Science*, *49*(2), 191–211. https://doi.org/10.1016/S0032-0633(00)00132-X

Harner, P. L., & Gilmore, M. S. (2015). Visible–near infrared spectra of hydrous carbonates, with implications for the detection of carbonates in hyperspectral data of Mars. *Icarus*, *250*, 204–214. https://doi.org/10.1016/j.icarus.2014.11.037

Hartmann, W. K., & Neukum, G. (2001). Cratering chronology and the evolution of Mars. In *Chronology and Evolution of Mars* (pp. 165–194). Springer. Retrieved from https://link.springer.com/chapter/10.1007/978-94-017-1035-0_6

Hausrath, E. M., Adcock, C. T., Bechtold, A., Beck, P., Brown, A., Cardarelli, E. L., et al. (2022). Examining soil crusts at Jezero crater, Mars. In *Presented at the 53rd lunar and planetary science conference (LPI contribution no. 1604)*.

Hoefen, T. M., Clark, R. N., Bandfield, J. L., Smith, M. D., Pearl, J. C., & Christensen, P. R. (2003). Discovery of olivine in the Nili Fossae region of Mars. *Science*, *302*(5645), 627–630. https://doi.org/10.1126/science.1089647

Holm-Alwmark, S., Kinch, K. M., Hansen, M. D., Shahrzad, S., Svennevig, K., Abbey, W. J., et al. (2021). Stratigraphic relationships in Jezero crater, Mars: Constraints on the timing of fluvial-lacustrine activity from orbital observations. *Journal of Geophysical Research: Planets*, *126*(7), e2021JE006840. https://doi.org/10.1029/2021JE006840

Horgan, B., Udry, A., Rice, M., Alwmark, S., Amundsen, H. E. F., Bell, J. F. III, et al. (2023). Mineralogy, morphology, and emplacement history of the Maaz formation on the Jezero crater floor from orbital and rover observations. *Journal of Geophysical Research: Planets*, *128*, e2022JE007612. https://doi.org/10.1029/2022JE007612

Horgan, B. H. N., Anderson, R. B., Dromart, G., Amador, E. S., & Rice, M. S. (2020). The mineral diversity of Jezero crater: Evidence for possible lacustrine carbonates on Mars. *Icarus*, *339*, 113526. https://doi.org/10.1016/j.icarus.2019.113526

Horgan, B. H. N., Cloutis, E. A., Mann, P., & Bell, J. F. (2014). Near-infrared spectra of ferrous mineral mixtures and methods for their identification in planetary surface spectra. *Icarus*, *234*, 132–154. https://doi.org/10.1016/j.icarus.2014.02.031

Hyvärinen, A., & Oja, E. (2000). Independent component analysis: Algorithms and applications. *Neural Networks*, *13*(4), 411–430. https://doi.org/10.1016/S0893-6080(00)00026-5

Irwin, R. P., Howard, A. D., Craddock, R. A., & Moore, J. M. (2005). An intense terminal epoch of widespread fluvial activity on early Mars: 2. Increased runoff and paleolake development. *Journal of Geophysical Research*, *110*(E12), E12S15. https://doi.org/10.1029/2005JE002460

Johnson, J. R., Bell, J. F., Bender, S., Blaney, D., Cloutis, E., DeFlores, L., et al. (2015). ChemCam passive reflectance spectroscopy of surface materials at the Curiosity landing site, Mars. *Icarus*, *249*, 74–92. https://doi.org/10.1016/j.icarus.2014.02.028

Johnson, J. R., Leget, C., Wiens, R. C., Newell, R. T., Cloutis, E., Forni, O., et al. (2022). Visible wavelength spectroscopy (400-1020 nm) of surface materials at Jezero crater, Mars, from Supercam and Mastcam-Z. In *Presented at the 53rd lunar and planetary science conference (LPI contribution no. 2678)*.

Klima, R. L., Pieters, C. M., & Dyar, M. D. (2007). Spectroscopy of synthetic Mg-Fe pyroxenes I: Spin-allowed and spin-forbidden crystal field bands in the visible and near-infrared. *Meteoritics & Planetary Sciences*, *42*(2), 235–253. https://doi.org/10.1111/j.1945-5100.2007.tb00230.x

Korablev, O. I., Dobrolensky, Y., Evdokimova, N., Fedorova, A. A., Kuzmin, R. O., Mantsevich, S. N., et al. (2017). Infrared spectrometer for ExoMars: A mast-mounted instrument for the rover. *Astrobiology*, *17*(6–7), 542–564. https://doi.org/10.1089/ast.2016.1543

Kreisch, C. D., O'Sullivan, J. A., Arvidson, R. E., Politte, D. V., He, L., Stein, N. T., et al. (2017). Regularization of Mars Reconnaissance Orbiter CRISM along-track oversampled hyperspectral imaging observations of Mars. *Icarus*, *282*, 136–151. https://doi.org/10.1016/j.icarus.2016.09.033

Kremer, C. H., Mustard, J. F., & Bramble, M. S. (2019). A widespread olivine-rich ash deposit on Mars. *Geology*, *47*(7), 677–681. https://doi.org/10.1130/G45563.1

Lantz, C., Poulet, F., Loizeau, D., Riu, L., Pilorget, C., Carter, J., et al. (2020). Planetary terrestrial analogues library project: 1. Characterization of samples by near-infrared point spectrometer. *Planetary and Space Science*, *189*, 104989. https://doi.org/10.1016/j.pss.2020.104989

Legett, C., Newell, R. T., Reyes-Newell, A. L., Nelson, A. E., Bernardi, P., Bender, S. C., et al. (2022). Optical calibration of the SuperCam instrument body unit spectrometers. *Applied Optics*, *61*(11), 2967–2974. https://doi.org/10.1364/AO.447680

Le Mouélic, S., Sotin, C., Combe, J. P., Ledeit, L., Gendrin, A., Mustard, J., et al. (2006). Composition of the dust on Mars derived from OMEGA hyperspectral images. In *Presented at the 37th annual lunar and planetary science conference (LPI contribution no. 1409)*.

Liu, Y., Tice, M. M., Schmidt, M. E., Treiman, A. H., Kizovski, T. V., Hurowitz, J. A., et al. (2022). An olivine cumulate outcrop on the floor of Jezero crater, Mars. *Science*, eabo2756. https://doi.org/10.1126/science.abo2756

Liu, Y., Wu, X., Zhao, Y.-Y. S., Pan, L., Wang, C., Liu, J., et al. (2022). Zhurong reveals recent aqueous activities in Utopia Planitia, Mars. *Science Advances*, *8*(19), eabn8555. https://doi.org/10.1126/sciadv.abn8555

Maki, J. M. (2021). *Mars 2020 hazard cameras bundle, raw products*. NASA Planetary Data System. https://doi.org/10.17189/282B-1524

Maki, J. N., Gruel, D., McKinney, C., Ravine, M. A., Morales, M., Lee, D., et al. (2020). The Mars 2020 engineering cameras and microphone on the Perseverance rover: A next-generation imaging system for Mars exploration. *Space Science Reviews*, *216*(8), 137. https://doi.org/10.1007/s11214-020-00765-9

Mandon, L. (2020). *Préparation des futures missions in situ martiennes via la télédétection et l'expérimentation en spectroscopie de réflectance*. (Doctoral thesis). University of Lyon. Retrieved from https://www.theses.fr/2020LYSE1261

Mandon, L., Beck, P., Quantin-Nataf, C., Dehouck, E., Pommerol, A., Yoldi, Z., et al. (2021). Martian meteorites reflectance and implications for rover missions. *Icarus*, *366*, 114517. https://doi.org/10.1016/j.icarus.2021.114517

Mandon, L., Beck, P., Quantin-Nataf, C., Dehouck, E., Thollot, P., Loizeau, D., & Volat, M. (2022). ROMA: A database of rock reflectance spectra for Martian in situ exploration. *Earth and Space Science*, *9*(1), e2021EA001871. https://doi.org/10.1029/2021EA001871

Mandon, L., Parkes Bowen, A., Quantin-Nataf, C., Bridges, J. C., Carter, J., Pan, L., et al. (2021). Morphological and spectral diversity of the clay-bearing unit at the ExoMars landing site Oxia Planum. *Astrobiology*, *21*(4), 464–480. https://doi.org/10.1089/ast.2020.2292

Mandon, L., Quantin-Nataf, C., Thollot, P., Mangold, N., Lozac'h, L., Dromart, G., et al. (2020). Refining the age, emplacement and alteration scenarios of the olivine-rich unit in the Nili Fossae region, Mars. *Icarus*, *336*, 113436. https://doi.org/10.1016/j.icarus.2019.113436

Mangold, N., Dromart, G., Ansan, V., Salese, F., Kleinhans, M. G., Massé, M., et al. (2020). Fluvial regimes, morphometry, and age of Jezero crater paleolake inlet valleys and their exobiological significance for the 2020 Rover Mission Landing Site. *Astrobiology*, *20*(8), 994–1013. https://doi.org/10.1089/ast.2019.2132

Mangold, N., Gupta, S., Gasnault, O., Dromart, G., Tarnas, J. D., Sholes, S. F., et al. (2021). Perseverance rover reveals an ancient delta-lake system and flood deposits at Jezero crater, Mars. *Science*, *374*(6568), eabl4051. https://doi.org/10.1126/science.abl4051

Mangold, N., Poulet, F., Mustard, J. F., Bibring, J.-P., Gondet, B., Langevin, Y., et al. (2007). Mineralogy of the Nili Fossae region with OMEGA/Mars Express data: 2. Aqueous alteration of the crust. *Journal of Geophysical Research*, *112*(E8), E08S04. https://doi.org/10.1029/2006JE002835

Manrique, J. A., Lopez-Reyes, G., Cousin, A., Rull, F., Maurice, S., Wiens, R. C., et al. (2020). SuperCam calibration targets: Design and development. *Space Science Reviews*, *216*(8), 138. https://doi.org/10.1007/s11214-020-00764-w

Massé, M., Bourgeois, O., Le Mouélic, S., Verpoorter, C., Le Deit, L., & Bibring, J. P. (2010). Martian polar and circum-polar sulfate-bearing deposits: Sublimation tills derived from the North Polar Cap. *Icarus*, *209*(2), 434–451. https://doi.org/10.1016/j.icarus.2010.04.017

Masursky, H. (1973). An overview of geological results from Mariner 9. *Journal of Geophysical Research*, *78*(20), 4009–4030. https://doi.org/10.1029/JB078i020p04009

Maurice, S., Clegg, S. M., Wiens, R. C., Gasnault, O., Rapin, W., Forni, O., et al. (2016). ChemCam activities and discoveries during the nominal mission of the Mars Science Laboratory in Gale crater, Mars. *Journal of Analytical Atomic Spectrometry*, *31*(4), 863–889. https://doi.org/10.1039/C5JA00417A

Maurice, S., Wiens, R. C., Bernardi, P., Caïs, P., Robinson, S., Nelson, T., et al. (2021). The SuperCam instrument suite on the Mars 2020 rover: Science objectives and Mast-unit description. *Space Science Reviews*, *217*(3), 47. https://doi.org/10.1007/s11214-021-00807-w

Maurice, S. A., & Wiens, R. C. (2021). *Mars 2020 SuperCam bundle*. NASA Planetary Data System. https://doi.org/10.17189/1522646

Merusi, M., Kinch, K. B., Madsen, M. B., Bell, J. F., III, Maki, J. N., Hayes, A. G., et al. (2022). The Mastcam-Z radiometric calibration targets on NASA's perseverance rover: Derived irradiance time-series, dust deposition, and performance over the first 350 sols on Mars. *Earth and Space Science*, *9*(12), e2022EA002552. https://doi.org/10.1029/2022EA002552

McEwen, A. S., Eliason, E. M., Bergstrom, J. W., Bridges, N. T., Hansen, C. J., Delamere, W. A., et al. (2007). Mars Reconnaissance Orbiter's High Resolution Imaging Science Experiment (HiRISE). *Journal of Geophysical Research*, *112*(E5), E05S02. https://doi.org/10.1029/2005JE002605

Meslin, P. Y., Forni, O., Beck, P., Cousin, A., Beyssac, O., Lopez-Reyes, G., et al. (2022). Evidence for perchlorate and sulfate salts in Jezero crater, Mars, from Supercam observations. In *Presented at the 53rd lunar and planetary science conference (LPI contribution no. 2694)*.

Milliken, R. E., & Bish, D. L. (2014). Distinguishing hisingerite from other Clays and its importance for Mars. In *Presented at the 45th lunar and planetary science conference (LPI contribution no. 2251)*.

Muirhead, B. K., Nicholas, A. K., Umland, J., Sutherland, O., & Vijendran, S. (2020). Mars sample return campaign concept status. *Acta Astronautica*, *176*, 131–138. https://doi.org/10.1016/j.actaastro.2020.06.026

Murchie, S., Arvidson, R., Bedini, P., Beisser, K., Bibring, J.-P., Bishop, J., et al. (2007). Compact reconnaissance imaging spectrometer for Mars (CRISM) on Mars reconnaissance orbiter (MRO). *Journal of Geophysical Research*, *112*(E5), 1–57. https://doi.org/10.1029/2006JE002682

Mustard, J. F., Ehlmann, B. L., Murchie, S. L., Poulet, F., Mangold, N., Head, J. W., et al. (2009). Composition, morphology, and stratigraphy of Noachian crust around the Isidis basin. *Journal of Geophysical Research*, *114*(E2), E00D12. https://doi.org/10.1029/2009JE003349

Mustard, J. F., Poulet, F., Gendrin, A., Bibring, J.-P., Langevin, Y., Gondet, B., et al. (2005). Olivine and pyroxene diversity in the crust of Mars. *Science*, *307*(5715), 1594–1597. https://doi.org/10.1126/science.1109098

Mustard, J. F., Poulet, F., Head, J. W., Mangold, N., Bibring, J.-P., Pelkey, S. M., et al. (2007). Mineralogy of the Nili Fossae region with OMEGA/Mars Express data: 1. Ancient impact melt in the Isidis basin and implications for the transition from the Noachian to Hesperian. *Journal of Geophysical Research*, *112*(E8), E08S03. https://doi.org/10.1029/2006JE002834

Ody, A., Poulet, F., Bibring, J.-P., Loizeau, D., Carter, J., Gondet, B., & Langevin, Y. (2013). Global investigation of olivine on Mars: Insights into crust and mantle compositions. *Journal of Geophysical Research: Planets*, *118*(2), 234–262. https://doi.org/10.1029/2012JE004149

Palumbo, A. M., & Head, J. W. (2018). Impact cratering as a cause of climate change, surface alteration, and resurfacing during the early history of Mars. *Meteoritics & Planetary Sciences*, *53*(4), 687–725. https://doi.org/10.1111/maps.13001

Poulet, F., Bibring, J.-P., Mustard, J. F., Gendrin, A., Mangold, N., Langevin, Y., et al. (2005). Phyllosilicates on Mars and implications for early Martian climate. *Nature*, *438*(7068), 623–627. https://doi.org/10.1038/nature04274

Poulet, F., Royer, C., Beck, P., Mandon, L., Quantin-Nataf, C., Johnson, J. R., et al. (2022). Modal mineralogy of Seitah unit in Jezero crater (Mars) retrieved from nonlinear unmixing analyses of IRS/SUPERCAM. In *Presented at the 53rd lunar and planetary science conference (LPI contribution no. 2032)*.

Quantin-Nataf, C., Holm-Alwmark, S., Lasue, J., Calef, F. J., Shuster, D., Kinch, K. M., et al. (2021). The complex exhumation history of Jezero crater floor unit. In *Presented at the 52nd lunar and planetary science conference (LPI contribution no. 2034)*.

Razzell Hollis, J., Moore, K. R., Sharma, S., Beegle, L., Grotzinger, J. P., Allwood, A., et al. (2022). The power of paired proximity science observations: Co-located data from SHERLOC and PIXL on Mars. *Icarus*, *387*, 115179. https://doi.org/10.1016/j.icarus.2022.115179

Rice, M. S., Johnson, J. R., Million, C. C., St. Clair, M., Horgan, B. N., Vaughan, A., et al. (2023). Spectral variability of rocks and soils on the Jezero crater floor: A summary of multispectral observations from *Perseverance's* Mastcam-Z instrument. *Journal of Geophysical Research: Planets*, *128*, e2022JE007548. https://doi.org/10.1029/2022JE007548

Roach, L. H., Mustard, J. F., Lane, M. D., Bishop, J. L., & Murchie, S. L. (2010). Diagenetic haematite and sulfate assemblages in Valles Marineris. *Icarus*, *207*(2), 659–674. https://doi.org/10.1016/j.icarus.2009.11.029

Rogers, A. D., Warner, N. H., Golombek, M. P., Head, J. W., III, & Cowart, J. C. (2018). Areally extensive surface bedrock exposures on Mars: Many are clastic rocks, not lavas. *Geophysical Research Letters*, *45*(4), 1767–1777. https://doi.org/10.1002/2018GL077030

Royer, C., Fouchet, T., Mandon, L., Montmessin, F., Poulet, F., Forni, O., et al. (2022). Reflectance of Jezero crater floor 1. Data processing and calibration of the infrared spectrometer (IRS) on SuperCam. *Journal of Geophysical Research: Planets*, e2022JE007481. https://doi.org/10.1029/2022JE007481

Scheller, E. L., & Ehlmann, B. L. (2020). Composition, stratigraphy, and geological history of the Noachian basement surrounding the Isidis impact basin. *Journal of Geophysical Research: Planets*, *125*(7), e2019JE006190. https://doi.org/10.1029/2019JE006190

Schon, S. C., Head, J. W., & Fassett, C. I. (2012). An overfilled lacustrine system and progradational delta in Jezero crater, Mars: Implications for Noachian climate. *Planetary and Space Science*, *67*(1), 28–45. https://doi.org/10.1016/j.pss.2012.02.003

Schröder, S., Meslin, P. Y., Gasnault, O., Maurice, S., Cousin, A., Wiens, R. C., et al. (2015). Hydrogen detection with ChemCam at Gale crater. *Icarus*, *249*, 43–61. https://doi.org/10.1016/j.icarus.2014.08.029

Shahrzad, S., Kinch, K. M., Goudge, T. A., Fassett, C. I., Needham, D. H., Quantin-Nataf, C., & Knudsen, C. P. (2019). Crater Statistics on the dark-toned, mafic floor unit in Jezero crater, Mars. *Geophysical Research Letters*, *46*(5), 2408–2416. https://doi.org/10.1029/2018GL081402

Simon, J. I., Amundsen, H. E. F., Beegle, L. W., Bell, J., Benison, K. C., Berger, E. L., et al. (2022). Sampling of Jezero crater Máaz formation by Mars 2020 Perseverance rover. In *Presented at the 53rd lunar and planetary science conference (LPI contribution no. 1294)*.

Stack, K. M., Williams, N. R., Calef, F., Sun, V. Z., Williford, K. H., Farley, K. A., et al. (2020). Photogeologic map of the Perseverance rover field site in Jezero crater constructed by the Mars 2020 Science Team. *Space Science Reviews*, *216*(8), 127. https://doi.org/10.1007/s11214-020-00739-x

Stopar, J. D., Jeffrey Taylor, G., Hamilton, V. E., & Browning, L. (2006). Kinetic model of olivine dissolution and extent of aqueous alteration on Mars. *Geochimica et Cosmochimica Acta*, *70*(24), 6136–6152. https://doi.org/10.1016/j.gca.2006.07.039

Thollot, P. (2013). Etude de l'altération de la surface de Mars par imagerie hyperspectrale: Minéralogie des régions de Noctis Labyrinthus et Valles Marineris (Doctoral dissertation). Retrieved from http://www.theses.fr/2013NANT2076

Tornabene, L. L., Moersch, J. E., McSween, H. Y., Hamilton, V. E., Piatek, J. L., & Christensen, P. R. (2008). Surface and crater-exposed lithologic units of the Isidis basin as mapped by coanalysis of THEMIS and TES derived data products. *Journal of Geophysical Research*, *113*(E10), E10001. https://doi.org/10.1029/2007JE002988

Tutolo, B. M., Evans, B. W., & Kuehner, S. M. (2019). Serpentine–hisingerite solid solution in altered ferroan peridotite and olivine gabbro. *Minerals*, *9*(1), 47. https://doi.org/10.3390/min9010047

Udry, A., Ostwald, A., Sautter, V., Cousin, A., Beyssac, O., Forni, O., et al. (2022). A Mars 2020 perseverance SuperCam perspective on the igneous nature of the Máaz formation at Jezero crater and link with Séítah, Mars. *Journal of Geophysical Research: Planets*, e2022JE007440. https://doi.org/10.1029/2022JE007440

Vaughan, A., Rice, M., Horgan, B., Johnson, J., Bell, J., Nunez, J., et al. (2021). A Mastcam-Z view of regolith at Jezero crater: Textural and spectral properties. In *Presented at the AGU fall meeting* (pp. P25I–P2245).

Viviano-Beck, C. E., Moersch, J. E., & McSween, H. Y. (2013). Implications for early hydrothermal environments on Mars through the spectral evidence for carbonation and chloritization reactions in the Nili Fossae region. *Journal of Geophysical Research: Planets*, *118*(9), 1858–1872. https://doi.org/10.1002/jgre.20141

Viviano-Beck, C. E., Seelos, F. P., Murchie, S. L., Kahn, E. G., Seelos, K. D., Taylor, H. W., et al. (2014). Revised CRISM spectral parameters and summary products based on the currently detected mineral diversity on Mars. *Journal of Geophysical Research: Planets*, *119*(6), 1403–1431. https://doi.org/10.1002/2014JE004627

Werner, S. C. (2008). The early Martian evolution—Constraints from basin formation ages. *Icarus*, *195*(1), 45–60. https://doi.org/10.1016/j.icarus.2007.12.008

Wiens, R. C., Maurice, S., Robinson, S. H., Nelson, A. E., Cais, P., Bernardi, P., et al. (2021). The SuperCam instrument suite on the NASA Mars 2020 rover: Body unit and combined system tests. *Space Science Reviews*, *217*(1), 4. https://doi.org/10.1007/s11214-020-00777-5

Wiens, R. C., Udry, A., Beyssac, O., Quantin-Nataf, C., Mangold, N., Cousin, A., et al. (2022). Compositionally and density stratified igneous terrain in Jezero crater, Mars. *Science Advances*, *8*(34), eabo3399. https://doi.org/10.1126/sciadv.abo3399

Wright, J., Barrett, A. M., Fawdon, P., Favaro, E. A., Balme, M. R., Woods, M. J., & Karachalios, S. (2022). Jezero crater, Mars: Application of the deep learning NOAH-H terrain classification system. *Journal of Maps*, 1–13. https://doi.org/10.1080/17445647.2022.2095935

Xu, W., Liu, X., Yan, Z., Li, L., Zhang, Z., Kuang, Y., et al. (2021). The MarSCoDe instrument suite on the Mars Rover of China's Tianwen-1 mission. *Space Science Reviews*, *217*(5), 64. https://doi.org/10.1007/s11214-021-00836-5

Yen, A. S., Gellert, R., Schröder, C., Morris, R. V., Bell, J. F., Knudson, A. T., et al. (2005). An integrated view of the chemistry and mineralogy of Martian soils. *Nature*, *436*(7047), 49–54. https://doi.org/10.1038/nature03637

Zaini, N., Van der Meer, F., & Van der Werff, H. (2012). Effect of grain size and mineral mixing on carbonate absorption features in the SWIR and TIR wavelength regions. *Remote Sensing*, *4*(4), 987–1003. https://doi.org/10.3390/rs4040987